Motion behaviour analysis of 18" ILT-structures

An installation procedure enhancement study

C.N. Westland

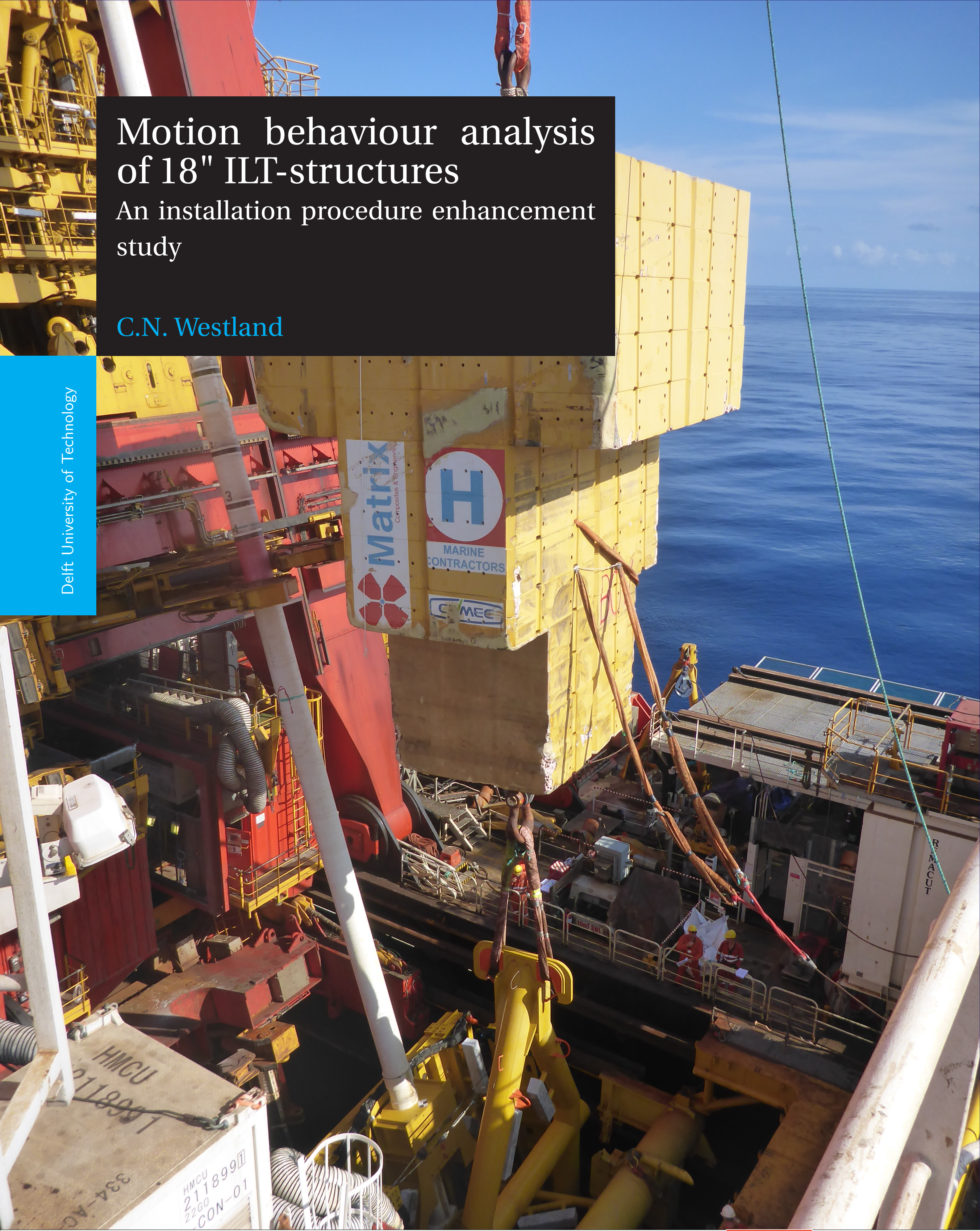

Delft University of Technology

Motion behaviour analysis of 18" ILT-structures

An installation procedure enhancement study

by

C.N. Westland

in partial fulfillment of the requirements for the degree of

Master of Science
in Offshore & Dredging Engineering

at the Delft University of Technology,
to be defended publicly on Thursday March 21, 2017 at 11:00 AM.

Supervisor:	Prof. Dr. A.V. Metrikine	TU Delft
Thesis committee:	Dr. Ir. P.R. Wellens	TU Delft
	Ir. J. Rodriguez Navarro	HMC
	Ir. H. Smienk	HMC

TU Delft — Delft University of Technology

PREFACE

Before you lies the thesis "Motion behaviour analysis of 18" ILT-structures". This is the result of the 9 month graduation internship I've done with Heerema Marine Contractors (HMC) for the conclusion of the master program Offshore & Dredging Engineering at the TU Delft.
Next to the fact I thoroughly enjoyed applying the knowledge I acquired during my studies, I feel enriched by the understanding I gained during this thesis trajectory. However, without the help of others, the results would not have been the same. Therefore, first of all I would like to thank my supervisors from HMC - Henk Smienk and Jesus Rodriguez Navarro - for the excellent guidance and willingness to share their experience with me. Whenever needed, I could rely on a helping hand and critical, but constructive feedback.
Secondly I would like to take the opportunity to express my gratitude to Peter Wellens, my daily supervisor from the TU Delft. Although I found difficulty in the academic process from time to time, his academic experience and bright view made that I could continue my work in the right direction. The same counts for Andrei Metrikine, my graduation professor. The interesting discussions during meetings and the ever-challenging questions kept me sharp along the way.
Additionally, and just as important, I must say I had a great time doing my thesis at HMC. From the moment I entered the office, I felt really welcome. The many discussions, activities, 'bakkies', but also the 'real' heavy-lifting sessions in the gym make for warm memories.
Finally, words can hardly describe how grateful I am with the family and friends surrounding me. Thank you all, you are amazing!
I sincerely hope you enjoy reading this. Good luck!

C.N. Westland
Delft, 14 March 2017

Abstract

220 miles offshore the West-Australian coast lies the Ichthys Field. In 2013 Heerema Marine Contractors (HMC) was contracted to install the umbilicals, risers and flowlines for the Ichthys Project, including the installation of several in-line structures such as in-line tees (ILT) and flow-line end terminations (FLET). The ship assigned to these installations was HMC's deep water construction vessel Aegir. Environmental loads, such as waves and currents, as well as vessel motions induce significant loads on the submerged structures and pipeline. These loads could impose high risks and damage to people and equipment when not completely controlled. Therefore, each installation step is thoroughly analysed. The main software package for these analyses is Flexcom, FEM software specialised on pipeline calculations.

The installation analysis of the 18" ILT-structure installations involved in the Ichthys project shows high compression in the upper- and upper-counter stem, the connection between the ILT and the pipe. Although Flexcom shows that buckling limits are exceeded, offshore load measurements of previous installations show hardly any compression.

By means of a sensitivity study, the Flexcom model has been investigated to determine the driving mechanism for compression. Varying several parameters, it was found that the compression in Flexcom was closely related to the wave kinematics, and thus to the hydrodynamic loads on any of the submerged structures (pipeline, ILT & weight-compensation buoy). Finally, the compression could be related to the hydrodynamic loading of the weight-compensation buoy. The reason for the discrepancy between the Flexcom calculations and offshore load measurements is the fact that the weight-compensation buoy is hanging in a moonpool. Flexcom does not account for the flow characteristics of the water in the moonpool and is, by taking the incident waves for hydrodynamic loads calculations, over-predicting the loads on the buoy. In operational conditions, water in the moonpool moves in a so-called piston mode, a purely vertical motion, and moves periodically with its resonance period.

In order to predict the water motions in the moonpool for future installations, 1,5 year of offshore motion measurements of the water in the moonpool have been compared to the incident wave field. Using this data, RAO's for water motions in the moonpool have been developed for each wave heading. From these RAO's it was found that the response of the moonpool is wave heading dependent; beam waves tend to excite water in the moonpool to a larger extend than waves reaching the bow or the stern. This relation is also observed in moonpool response calculations with diffraction software (WAMIT). Knowing the moonpool is excited by pressure fluctuations at the inlet of the moonpool, the pressure distribution around barge models of varying lengths has been studied. It was found that the distance between the hull side and the moonpool is a governing parameter for the response of the moonpool, but in case the moonpool is located close to the side, pressure interference patterns along the hull could both in- or decrease the excitation. This interference occurs at hull lengths of a multiple of the incoming wave length.

Using the acquired knowledge from both literature and measurements, two new analysis procedure are proposed for structure installations through a moonpool. The first procedure uses incident waves for the vessel motion calculation, but uses a separately defined moonpool motion spectrum for the calculation of hydrodynamic loads on the buoy. However, due to the assumption of empty-moonpool conditions and the exponential decrease of wave kinematics over depth, this procedure yields some inaccuracies. The second procedure comprises the application of a user-defined load time-trace on the submerged structure, which is generated from non-empty moonpool measurements or CFD-results. Although the second procedure is more accurate, both procedures have shown to well approximate the loads measured offshore.

Further research should be done on object-specific water motion characteristics of the moonpool.

Glossary

CFD Computational Fluid Dynamics.

COG Centre of Gravity.

DCV Deepwater Construction Vessel.

DNV Det Norske Veritas.

DP Dynamic Positioning.

FEM Finite Element Method.

FLET Flowline End Termination.

HMC Heerema Marine Contractors.

ILS In-line structure.

ILT In-line tee.

KC Keuligan-Carpenter.

RAO Response Amplitude Operator.

Nomenclature

α_{3D}	3D correction factor	$-$
κ	Coefficient for considering increased draft	$-$
ω_0	Undamped natural frequency	Hz
ω_r	Resonance frequency	Hz
ρ	Specific density of sea water	$\frac{kg}{m^3}$
θ	Wave direction	$^\circ$
ζ	Damping ratio	$-$
A	Cross-sectional area of the moonpool	m^2
A_{body}	Cross-sectional area of the body	m^2
A_{body}/A	Moonpool blockage factor	$-$
a_m	Added mass coefficient from potential theory	kg
A_p	Projected area perpendicular to the flow	m^2
b_1	Damping coefficient from potential theory	$\frac{kg}{s}$
b_2	Quadratic damping coefficient	$\frac{kg}{m^2}$
b_{eq}	Equivalent linearized damping coefficient	$\frac{kg}{s}$
C_0	Constant damping coefficient	$-$
C_1	Linear damping coefficient	$-$
C_2	Quadratic damping coefficient	$-$
C_{A0}	Added mass coefficient for unrestricted flow	$-$
C_A	Added mass coefficient	$-$
C_{D0}	Drag coefficient for unrestricted flow	$-$
C_D	Drag coefficient	$-$
C_M	Inertia coefficient ($C_A + 1$)	$-$
D	Characteristic diameter	m
d_{hz}	Added mass interaction coefficient	kg
E_f	Spectral energy per frequency	$\frac{m^2}{Hz}$
e_{hz}	Damping interaction coefficient	$\frac{kg}{s}$
F_{wh}	Wave force exciting h	N
g	Gravitational acceleration	$\frac{m}{s^2}$
H	Draft of the moonpool	m

h	Relative motion in the moonpool	m
h_{abs}	Absolute motion of the water in the moonpool	m
k_{hyd}	Hydrostatic stiffness	$\frac{N}{m}$
KC	Keuligan-Carpenter number	$-$
L	Longitudinal dimension of the object	m
M	Total water mass in the moonpool	kg
T	Motion period	s
T_n	natural period	s
u_a	Water velocity amplitude	$\frac{m}{s}$
V_r	Reference volume of the body	m^3
z	Heave motion	m

SIGN CONVENTIONS

WAVE DIRECTION

As the focus of this thesis is the enhancement of a Flexcom analysis procedure, it is chosen to use the sign conventions and axis system of Flexcom. Therefore, when not explicitly stated, wave directions are referred to as the wave heading with respect to the lay-direction of DCV Aegir. A visualization of the wave heading conventions is depicted in figure 1.

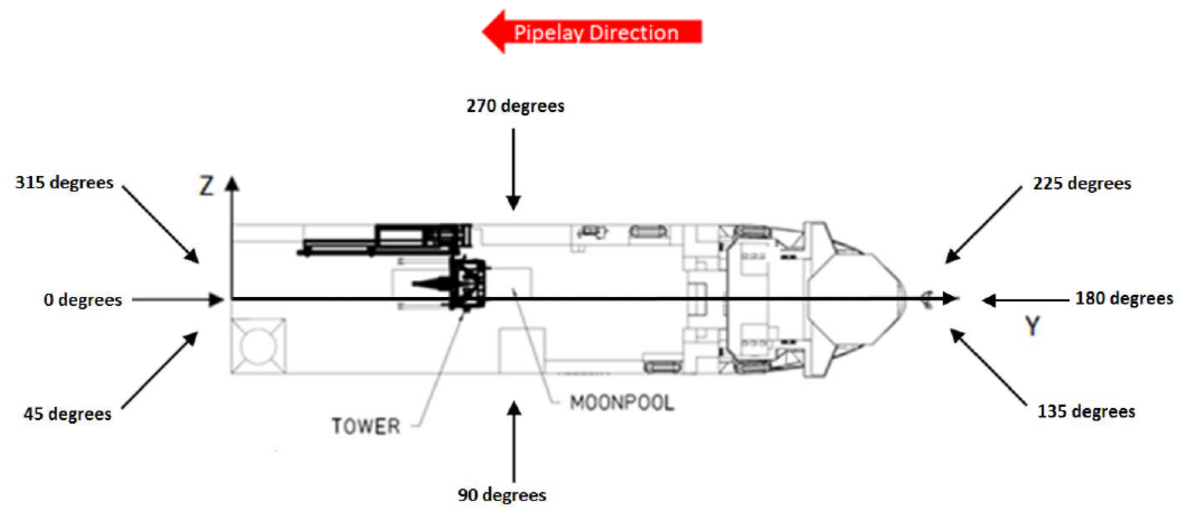

Figure 1: Current and wave directions w.r.t. DCV Aegir

These directions are based on the Flexcom axis system.

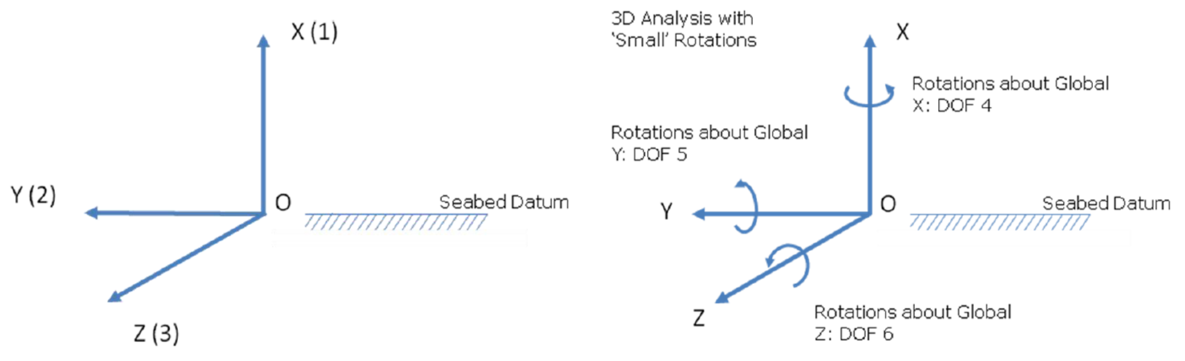

(a) Translational degrees of freedom (b) Rotational degrees of freedom

Figure 2: Flexcom axes

LOADS

Standard sign convention from fundamental structural mechanics are used with respect to the load calculations in this thesis. This means that positive loads are referred to as tensional loads, while compressive loads are characterized by a negative sign as shown in figure 3

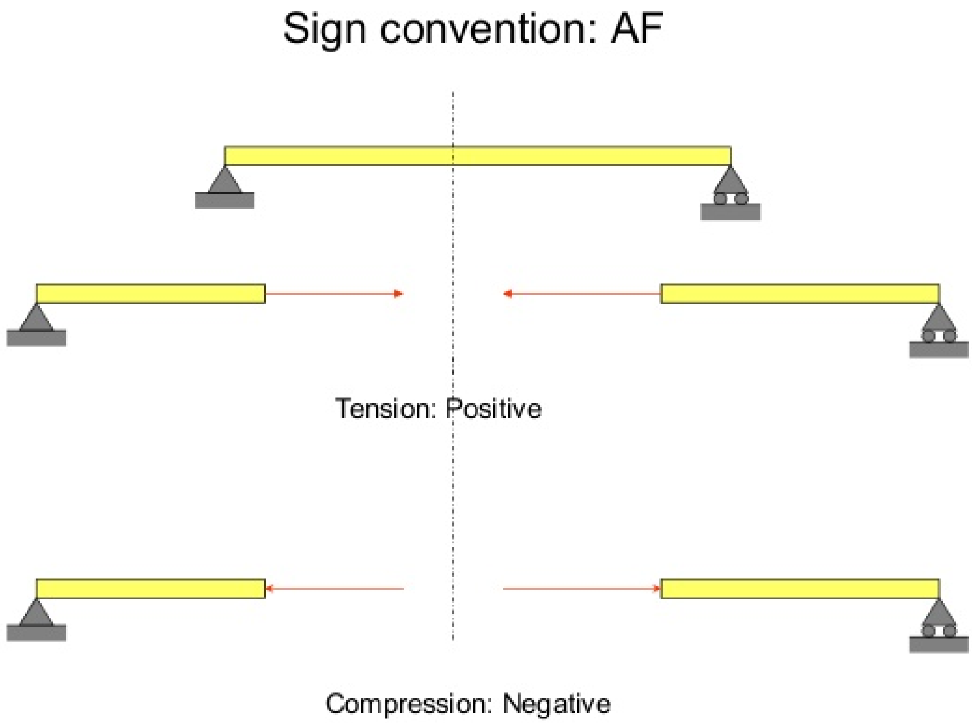

Figure 3: Sign conventions w.r.t. loads

Contents

Preface iii

Abstract v

Glossary vii

Nomenclature ix

Sign conventions xi

1 Introduction 1
- 1.1 General background . . . 1
- 1.2 Problem description . . . 2
- 1.3 Objective . . . 3
- 1.4 Problem approach . . . 3
- 1.5 Report outline. . . . 3

2 Model investigation 5
- 2.1 Original analysis set-up . . . 5
- 2.2 Static analysis and current . . . 6
- 2.3 Waves . . . 7
- 2.4 Vessel dynamics. . . . 7
- 2.5 Load investigation . . . 9
- 2.6 Structure dynamics . . . 9

3 Literature 11
- 3.1 Moonpool motion behaviour . . . 11
- 3.2 Resonance . . . 13
  - 3.2.1 Mass-spring system . . . 13
  - 3.2.2 Potential theory . . . 13
- 3.3 Model tests . . . 14
  - 3.3.1 Scale model . . . 14
  - 3.3.2 CFD model. . . . 15
- 3.4 Structures in the moonpool . . . 16
  - 3.4.1 Morison's equation. . . . 16
  - 3.4.2 Moonpool influence . . . 18
  - 3.4.3 Inertia & drag dominance . . . 18
  - 3.4.4 Structure influence. . . . 19

4 Moonpool measurements 21
- 4.1 Wave motions. . . . 21
  - 4.1.1 Incoming waves . . . 21
  - 4.1.2 Moonpool water motions . . . 22
- 4.2 Moonpool RAO's . . . 22
- 4.3 Viscous damping . . . 24
- 4.4 Wave heading dependency . . . 24
- 4.5 Structure effect . . . 30

5 Model enhancement 33
- 5.1 Moonpool implementation . . . 33
  - 5.1.1 Model 1: Empty moonpool conditions . . . 33
  - 5.1.2 Model 2: Non-empty moonpool conditions . . . 34

5.2 Additional changes . . . 35
5.2.1 Horizontal damping . . . 35
5.2.2 Hydrodynamic coefficients . . . 36
5.3 Validation . . . 36
5.3.1 Model configuration . . . 36
5.3.2 Results . . . 37
5.3.3 Original configuration check . . . 38
5.4 Current influence . . . 38
5.5 Workability . . . 39

6 Conclusions and recommendations **41**
6.1 Conclusion . . . 41
6.1.1 Moonpool . . . 41
6.1.2 Model enhancement . . . 42
6.2 Recommendations . . . 42

Bibliography **43**

A RAO calculations **45**
A.1 Incoming wave spectrum . . . 45
A.2 Moonpool wave spectrum . . . 45
A.2.1 Data filter . . . 45
A.2.2 RAO function . . . 46

B Free surface and hull pressures of WAMIT barge **49**

List of Figures **51**

List of Tables **53**

1

INTRODUCTION

1.1. GENERAL BACKGROUND

220 kilometers offshore the West-Australian coast lies the Ichthys Field. With an expected production capacity of 8.9 million tonnes of LNG per annum, 1.6 million tonnes of LPG per annum and an additional 100.000 barrels of condensate per day at it's peak, it is one of the biggest hydrocarbon liquids fields in Australia. By the use of a FPSO, most of the produced condensate is directly processed and distributed around the world, while the produced gas is being transported through one of the worlds longest subsea gas export lines to an onshore processing facility in Darwin 890 kilometers down the coast.
In 2013 Heerema Marine Contractors (HMC) was contracted in order to install the umbilicals, risers and flowlines for the Ichthys project, including the installation of several In-line structures (ILSs) such as In-line tees (ILTs) and Flowline End Terminations (FLETs). The ship assigned to these installations was HMC's new Deepwater Construction Vessel (DCV) Aegir. Equipped with a 4000 mT crane, together with a J- & R-lay tower, DCV Aegir is able to install pipelines and structures up to a water depth of 3500 m.

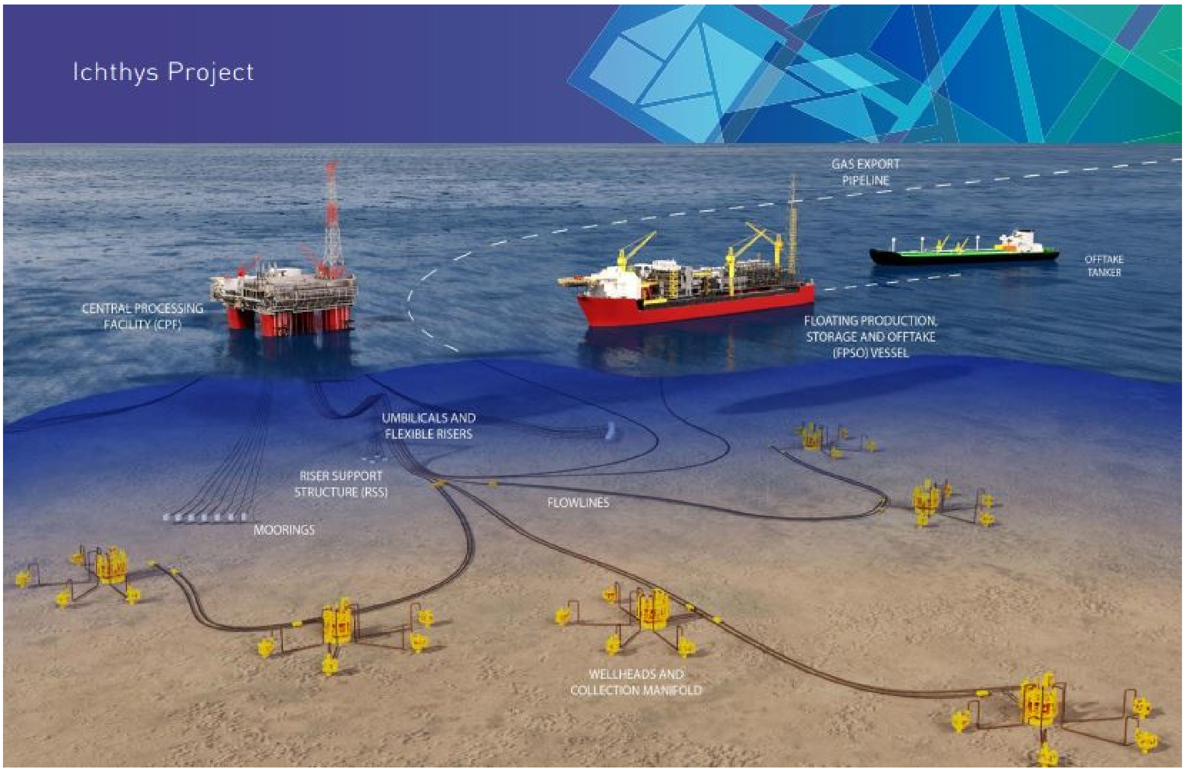

Figure 1.1: Ichthys field

1.2. PROBLEM DESCRIPTION

During the entire project span DCV Aegir has, among other ILSs, installed 6 ILTs. Environmental loads, as well as vessel motions induce significant forces on both the vessel and submerged structures, which accordingly translates to loads in the crane and pipelay tower. These loads could impose high risks and damage to people and equipment when not completely controlled. Therefore each installation step has to be thoroughly analysed and checked on whether allowable stresses are not being exceeded.
The 18" ILT-structures being used in the Ichthys field are of such dimensions and weight that they push DCV Aegir to its limits. The procedure includes upending these 200 mT structures, lowering them through the moonpool and connecting a 150 mT buoyancy module to the ILT. This made these installations the most complicated job for DCV Aegir so far, which also required complex analyses and models to be created.
Pipeline installation analyses generally involve the use of Flexcom and Abaqus, both Finite Element Method (FEM)-packages specialized on stress calculations in pipelines. By including forecasted and design sea states in the models, insight is acquired about the workability of these specific operations.
During the analyses of the 18" ILT-installations, high compressive loads were observed in the upper stem of the ILTs in several steps of the installation. Compression in the pipeline, together with bending loads, could lead to buckling of the pipe and has to be kept within limits all time. To do so, the driver for these compressive loads has to be controlled. Although modelled and investigated in detail, it was still not clear which mechanisms were causing these loads. Real-time force measurements in the upper stem of the ILT hardly show any compression.

The particular configuration in which high compression is observed in the model occurs when the ILT is hanging beneath the vessel and is supported by the 150 mT weight compensation buoy. As can be seen in Figure 1.2, at this stage the buoy is in the moonpool just below the water surface, but still connected to the crane. The buoy compensates for the weight of the submerged ILT, but doesn't account for the weight of the catenary. This load is therefore still carried by the crane. In the next step, the catenary load will be transferred to the travelling block, but in order to do so, the travelling block has to be closed first. This short time frame, when the catenary is still carried by the crane, and also connected to the travelling block leads to a critical load case.

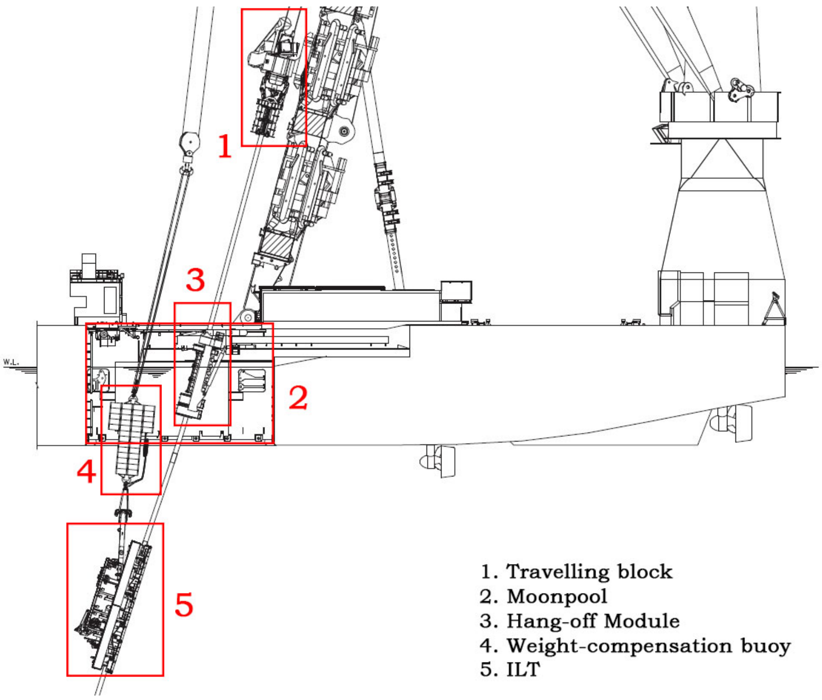

Figure 1.2: ILT with buoyancy module

1.3. OBJECTIVE

The model being used to analyse the installation of 18" ILT-structures predicts high compressive loads to be present in the upper- and uppercounter stem during the ILT-load transfer from the crane to the travelling block. These loads can cause local and/or global buckling criteria to fail, which means that the installation cannot be carried out in prevailing sea states. This drastically reduces the workability, resulting in a limited weather window that is suitable for this installation. Comparisons with offshore measurement show that the model is probably too conservative and should therefore be improved. This leads to the objective of this thesis:

"Increase the understanding of mechanisms leading to compression in the upper- and uppercounter stem during 18" ILT-installations and improve the model to increase workability."

1.4. PROBLEM APPROACH

In order to reach the goal - improving the model and in the end increasing workability - the following approach is taken:

1. Understand the model; Find out which calculations are performed and which assumptions are utilized.
2. Find the driver for compression in the upper- and uppercounter stem by using a sensitivity analysis. Investigate how the model reacts on changing different parameters.
3. Investigate whether the model component leading to compression is modelled correctly by means of a literature study.
4. Improve the model by implementing the findings from item 3 into the model.
5. Verify the improved model by comparing the results of the new model to offshore measurements.

The acquired new model and knowledge should lead to a decrease in loads when analysing the ILT-structure procedure. Consequently, the allowable environmental limits will increase. Recommendations on the interpretation of these new allowables will be given.

1.5. REPORT OUTLINE

The structure of this report is set-up in the chronological order of the research. It starts with the investigation of the model that led to the compression issue. After the model has been analysed systematically and the driver for compression in the upper stem has been found, an extensive literature study is done, focussing on this mechanism and how to implement this into the existing model. Subsequently, offshore measurement data is collected to gain additional knowledge for a realistic implementation. In chapter 5 the existing model is enhanced according to the acquired knowledge, after which the improved model is validated by offshore measurement. Finally, conclusions and recommendations are given on the conducted research.

2

Model investigation

In order to determine the driving mechanism for compression in the upper stem of the ILT, the model is taken apart systematically. The first step in this procedure is the investigation of the Flexcom, the software package which is used for the analysis of structure installations.

2.1. Original analysis set-up

The software package that is being used to determine global loads and strains in the pipeline during installations is Flexcom. Flexcom incorporates vessel motions and wave loads on the pipeline and structures and is able to calculate both the static and dynamic behaviour of the system by means of FEM. In order to calculate the loads and motions to be expected offshore, several design sea states, as well as governing current profiles, are selected for several installation headings. During the first phase of the analysis, the static equilibrium of the system is calculated. At this stage loads, motions and strains should stay within allowable limits. The static analysis consist of two parts: first, the system is only subject to gravitational loads. The ship is fixed in position, but the pipeline will try to find a static equilibrium iteratively. Once static equilibrium is found, static loads resulting from a constant current profile are applied. If a new equilibrium is found and the loads are within allowable limits, the analysis can proceed to the next step; the dynamic analysis. Once the static equilibrium passes the requirements, the most critical stages in the installation are selected to be subjected to the dynamic load case. Waves from different directions are applied for 20 minutes. The most severe conditions, based on maximum loads in the system, are subsequently simulated for a second time, but now for a time-span of 3 hours.

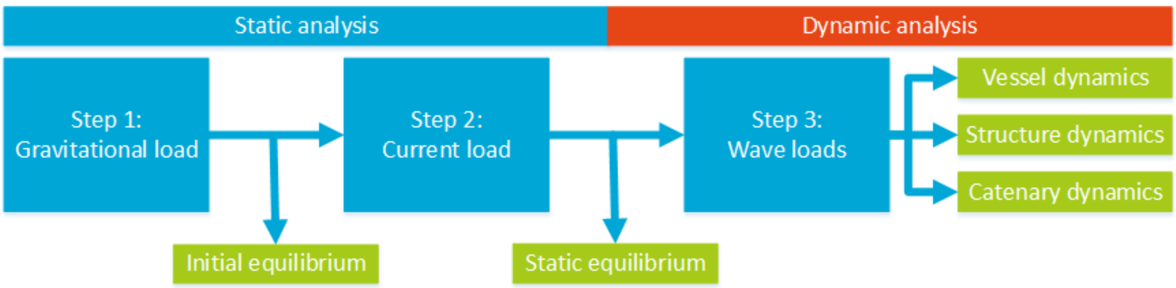

Figure 2.1: Standard analysis procedure

As stated, the critical load case during the 18" ILT-structures was when the ILT is hanging beneath the vessel and is both connected to the buoy/crane and the travelling block. This configuration is depicted in figure 2.2 and is the model representation of figure 1.2. During the first phase of the analysis - the static check -, the resulting loads are as expected. The static load in the upper stem at this point is 14 mT of compression. This compression is due to the self weight of the pipeline between the ILT and the travelling block. However, during the second phase, where environmental loads are included in the model, the load in the connection between the pipe and the ILT, the upper stem, comprise compression peaks up to 30 mT for encountered sea

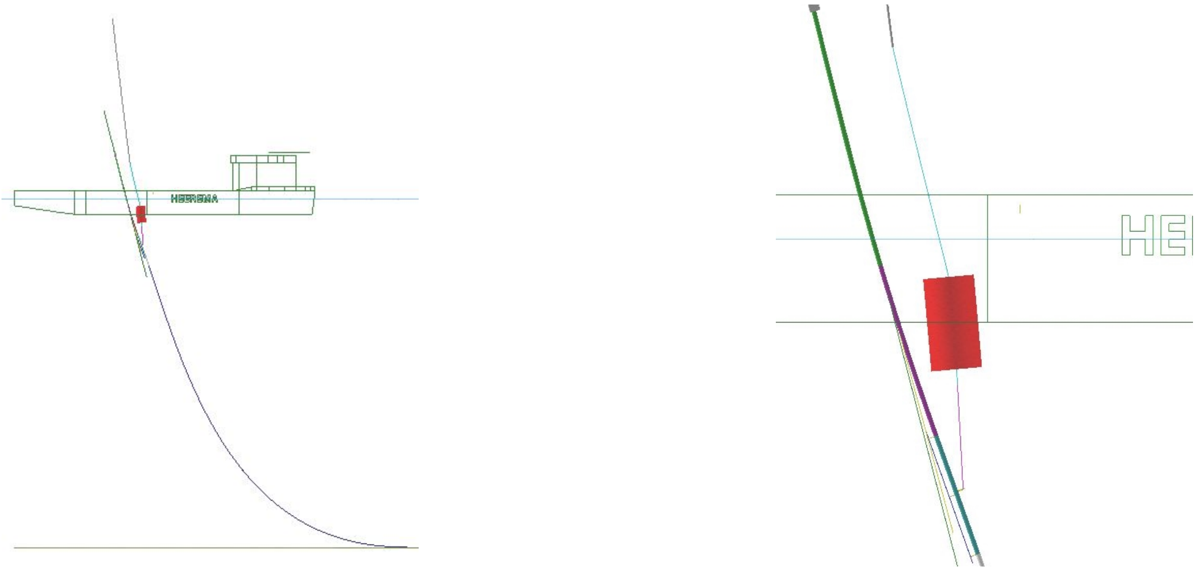

(a) Overview (b) Buoy and ILT

Figure 2.2: Flexcom model

states and peaks up to 80 mT for design sea states.
Especially the results where an encountered sea state is used in the model are remarkable. The load measurements during the ILT-installation where this sea state was measured is shown in Figure 2.3. As can be seen from the line representing the load in the travelling block, no severe compression peaks are observed. It should be noted that this load is measured in the travelling block itself, while the critical loads in the Flexcom model occur in the part between the ILT and the upper stem. Hence a static difference of 14 mT of compression. However, adding up the 14 mT of compression to the measured signal still does not increase the compression to the 30 mT predicted by Flexcom. In order to get a better understanding of why the Flexcom model differs from offshore measurements, it should be known how Flexcom calculates the different loads and motions of the system. The following sections will evaluate these calculations.

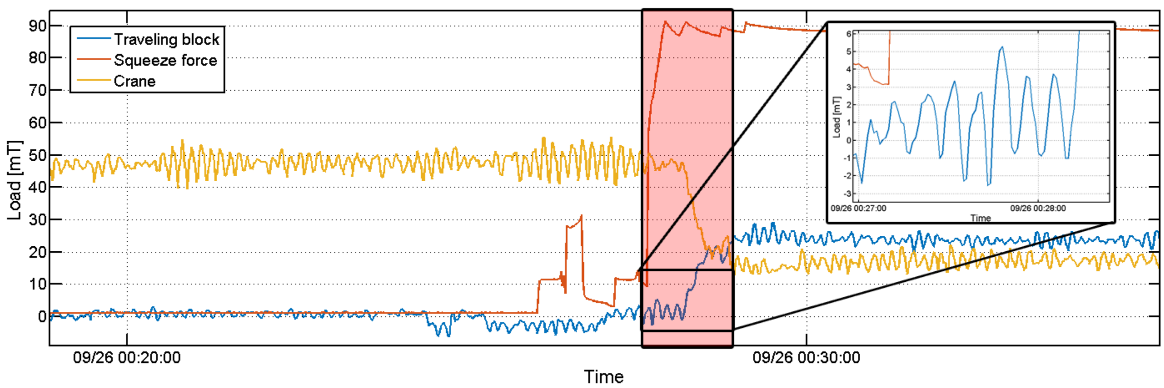

Figure 2.3: Offshore measurements

2.2. STATIC ANALYSIS AND CURRENT

As stated, the first step of the static analysis is in accordance with offshore load measurements. However, currents could lead to significant loads. This load is assumed to be constant and can therefore be included in the static analysis. For the ILT-installation analysis a constant unidirectional current profile of 0.4 m/s is used. To investigate the influence of the current on the static load in the upper stem, the current is applied from 3 different direction: 0°, 90°and 180 °. The results of the current sensitivity is depicted in figure 2.4. Although the current speeds are reasonable, the static offset induced by these currents are large. The difference between the yellow line (no current) and the most severe current direction, 180°, yields 18 mT. Although this is a significant difference, the observed compression peaks are the result of dynamic effects. The focus will be on the driving mechanism behind these peaks. Therefore, for the remainder of this model investigation, the current influence will be neglected.

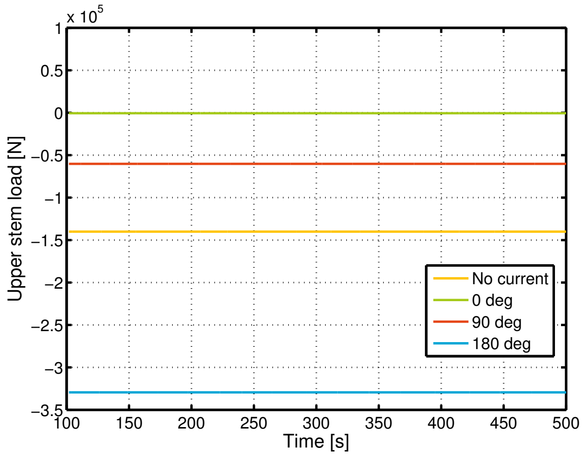

Figure 2.4: Current influence for different directions

2.3. WAVES

In general, for the analysis of installations using Flexcom, so-called design sea-states are used. The first step in the selection of design states is defining the prevailing characteristics of waves in the particular installation area. Sea-states with these characteristics are imposed on the vessel in a hydrodynamic analysis. In order to maximize the operational efficiency, the following limiting criteria for DCV Aegir are defined:

-

The sea-states resulting in responses within these indicative limiting criteria are subsequently used for the pipe-lay installation analysis in Flexcom. However, these are not necessarily the limiting sea-states. If the design sea-states result in pipeline integrity failure, the sea-states are reduced until the pipeline integrity is obtained again. These are the operational limiting criteria.
For the analysis of the 18" ILT installation during the Ichthys project a similar procedure has been used and design sea states have been selected. These sea-states can be found in appendix **??**. Although these design sea-states have been used for the original pipe-lay analyses, in this thesis, measured sea-states during executed installations are used to compare the Flexcom results to reality. Sea-states can be either defined by one or more standard spectra, such as a JONSWAP spectrum, or by a user-defined spectrum. Using the first option, Flexcom generates a spectrum according to the spectrum parameters:

- Peak frequency
- Peakedness
- Wave direction with respect to the vessel heading
- Phillip's constant

In case a user-defined spectrum is chosen, separate frequency components with the according spectral energy values have to be defined manually by the user.

2.4. VESSEL DYNAMICS

An important part of the dynamics of the model are the vessel motions. Vessel motions are caused by pressure differences around the hull coming from the waves. Therefore, to accurately calculate vessel motions the interaction between the waves and the vessel should be known. By means of potential flow theory and CFD-calculations this can be done, but as these calculations are computationally expensive, Flexcom uses predefined Response Amplitude Operator (RAO)'s to calculate the motions of the vessel. These RAO's describe the relation between the encountered wave spectrum and the motion response of the ship[1] (eq. 2.1).

$$S_{vessel} = S_{wave} * RAO^2 \tag{2.1}$$

As vessel motions are continuously registered by sensors aboard the Aegir, the motions calculated by Flexcom can be validated. The waves used by Flexcom to calculate motions of the vessel are randomly generated from a user-defined spectrum by means of a Monte-Carlo simulation and are only similar to the measured sea state in the frequency domain. Therefore the comparison of the vessel motions also has to be done in the frequency domain. To do so, both the motion time traces from Flexcom and motions measured offshore will be transformed to the frequency domain by using the Fourier transform. The critical ship motions for pipeline installation are heave, pitch and roll. The remaining three motions – surge, sway and yaw – are considered to be compensated by the Dynamic Positioning (DP)-system.

The resulting spectral density plots from Flexcom are compared with offshore measurements by their statistical values, the peak frequency and standard deviation. These values are shown in table 2.1. As expected, the vessel motions in Flexcom do well compare to the vessel motions that have been measured offshore. The RAO's of DCV Aegir have been calculated by means of diffraction software and validated by model tests and should be rather accurate. This comparison shows that the way Flexcom calculates the vessel motions is acceptable.

	Flexcom	Offshore
Heave	$\sigma =$	$\sigma =$
	$f_{peak} =$	$f_{peak} =$
Roll	$\sigma = °$	$\sigma = °$
	$f_{peak} =$	$f_{peak} =$
Pitch	$\sigma = °$	$\sigma = °$
	$f_{peak} =$	$f_{peak} =$

Table 2.1: Vessel motion comparison between Flexcom and offshore measurements

Assuming the vessel motions are not over- or underpredicted by Flexcom, the vessel motions most probably are not the driver for compression in the upper stem. Consequently, if the RAO's of the vessel are left out during the simulation, similar compressive peaks should be observed in the upper stem. To confirm this, a simulation has been done without vessel motions. As can be seen from the result in figure 2.5, vessel motions do hardly influence the compression in the upper stem.

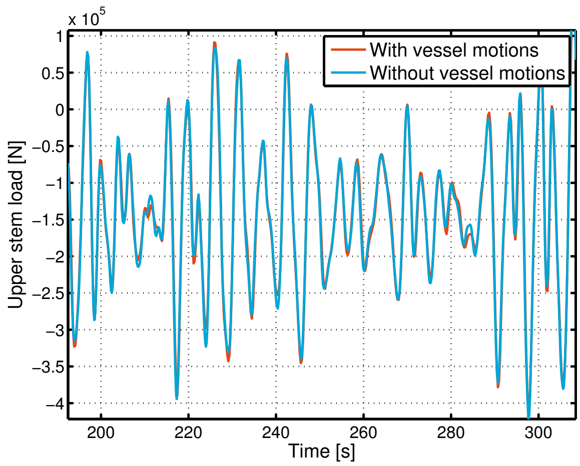

Figure 2.5: Vessel motion influence on the load in the upper stem

2.5. LOAD INVESTIGATION

A few mechanisms can be determined for the excitation of the system:

1. Vessel motions
2. Dynamic behaviour of the submerged structures
3. Dynamic behaviour of the catenary

As the vessel motions are considered to be correctly predicted by Flexcom, the second step in the investigation is identifying the characteristics of the calculated load. Due to the fact that the load in the travelling block is probably induced by several loading mechanisms, it is hard to find similarities between time traces. Additionally, potential phase differences between the excitation and the load induce shifts in the signal, which makes it even more complex. However, by using a Fourier transform, the spectral components of the load can be identified. Excitation mechanisms with energy in the same spectral range could be the driver for compression.

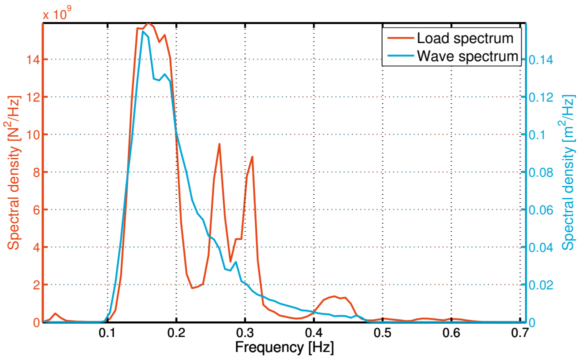

Figure 2.6: Spectral density plots of the upper stem load and the design wave spectrum

In figure 2.6 the spectral density plot of the upper stem load is represented by the red line. For this investigation, the original analysis model including a design sea-state, has been used. The wave spectrum defined in this model is a JONSWAP spectrum with a peak frequency of 0.16 Hz. As a similar trend in the spectral density of the load is observed, it has been chosen to depict the wave spectrum in the same figure. This spectrum is represented by the blue line and indeed shows similarities with the load spectrum. With only the dynamics of the catenary and the submerged structures left as possible drivers for compression, this is plausible. These are all excited by direct hydrodynamic interaction with the waves.

2.6. STRUCTURE DYNAMICS

Assuming the diameter of the catenary is small compared to the submerged structures – the buoy and the ILT – the next step is to investigate the sensitivity of the upper stem load with respect to these submerged structures. A similar approach is taken as done with the vessel motions. To exclude hydrodynamic loading of these structures from the simulation, the hydrodynamic coefficients of one of the structures is set to zero. This is at first done with the ILT and secondly with the buoy.

Setting the hydrodynamic coefficients of the ILT to zero does affect the compression in the upper stem, but still high compressive loads are observed (figure 2.7a). However, when the properties of the buoy are set to zero, the compression in the upper stem almost disappears completely (figure 2.7b). This clearly indicates that the driver for compression is the loading of the buoy. A discrepancy in the modelling of the buoy in Flexcom is evident and has to be investigated.

Since, Flexcom does not take into account diffraction, the waves encountered by the buoy are undisturbed. Due to the presence of the hull and the fact that the buoy is hanging in the moonpool, the wave induced motions of the buoy are completely different in reality. How the water is moving at the location of the moonpool will be studied in chapter 3.

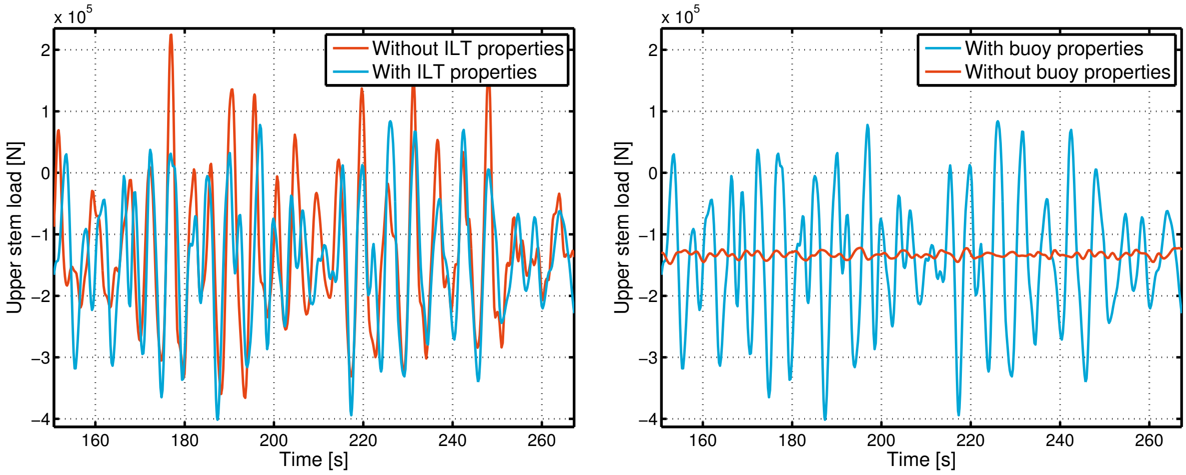

(a) ILT sensitivity

(b) Buoy sensitivity

Figure 2.7: Effect of the hydrodynamic loading of the submerged structures on the upper stem compression

3
LITERATURE

As follows from chapter 2, the original Flexcom model is not suitable for calculations with structures hanging in the moonpool. The water in a moonpool shows different behaviour from the waves outside of the DCV Aegir. As the loads on the structure are induced by the water motions in the moonpool, loads are not predicted correctly. Not only due to the moonpool itself water motions in the moonpool are different, the water motions are also affected by objects being present in the moonpool. In order to determine how to implement the moonpool in Flexcom realistically, a literature study has been done on the water motion behaviour in the moonpool, model tests that have been conducted and how structure loads are related to water motions in the moonpool.

3.1. MOONPOOL MOTION BEHAVIOUR

Although the water in the moonpool is moving in an oscillatory manner, the water is moving different from normal sea waves. Depending on whether the ship is moving or not, the water in the moonpool tends to move in a certain mode. In stationary conditions this mode is a piston-like motion, which means that the water can only move vertically. Horizontal water motions are not possible due to the walls of the moonpool. However, when the ship is moving, a pressure and friction gradient at the inlet of the moonpool caused by the horizontal ship velocity, causes the water in the moonpool to move in a so called sloshing mode. In this mode, the water is moving horizontally in between the walls of the moonpool. As the pipelay installation is considered to by a stationary process, the focus of this study will be on the piston mode. The modes of the moonpool occur at specific frequencies and can, if loading conditions are right, show typical resonance behaviour. This means that large relative motions, up to four times the incoming wave height, can occur in the moonpool. This could pose a potential danger to equipment and crew and should therefore be avoided.

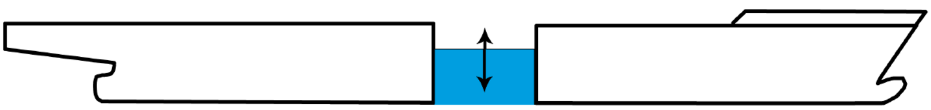

(a) Piston mode

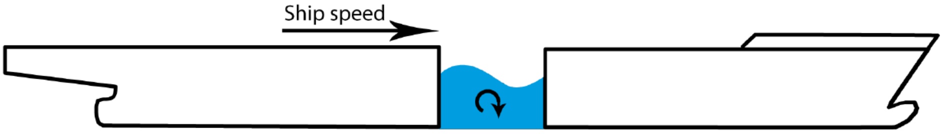

(b) Sloshing mode

Figure 3.1: Resonance modes of the moonpool

In stationary condition, the water in the moonpool is behaving like one vertically, periodically moving mass. Aalbers [2] stated that it can therefore be approached as a single mass-spring system , with the water acting as the mass and the hydrostatic stiffness acting as a spring. By means of energy conservation he derived the total equation of motion for a free floating body with a moonpool at the Centre of Gravity (COG) (3.1). The water in the moonpool is excited by pressure fluctuations at the inlet of the moonpool. These pressure variations are caused by the incoming waves, wave reflection and ship motions. In particular the heave, roll and pitch motion of the ship induce pressure variations on the hull. Most of the moonpools however, including the moonpool of the DCV Aegir, are located close to the ship COG. Consequently, only the heave motion of the ship affect the hull pressure variations at the inlet of the moonpool.

$$\begin{aligned} &\left(\rho A(H+h)+a_m\right)\ddot{h}+b_1\dot{h}+b_2\dot{h}\left|\dot{h}\right|+\rho g A h+ \\ &+\left(d_{hz}+\rho A(H+h)+a_h\right)\ddot{z}+\left(e_{hz}+b_1\right)\dot{z}+\rho g A z+ \\ &\qquad\qquad +\text{higher order terms}=F_{wh} \end{aligned} \tag{3.1}$$

where

ρ :Specific density of sea water $[\frac{kg}{m^3}]$
A :Cross-sectional area of the moonpool $[m^2]$
H :Draft of the moonpool $[m]$
h :Relative motion in the moonpool $[m]$
a_m :Added mass coefficient from potential theory $[kg]$
b_1 :Damping coefficient from potential theory $[\frac{kg}{s}]$
b_2 :Quadratic damping coefficient $[\frac{kg}{m^2}]$
g :Gravitational acceleration $[\frac{m}{s^2}]$
d_{hz} :Added mass interaction coefficient $[kg]$
e_{hz} :Damping interaction coefficient $[\frac{kg}{s}]$
z :Heave motion $[m]$
F_w :Wave force $[N]$

The first line of the equation is related to the hydrodynamic aspects of the moonpool itself, with h the water motion relative to the ship. The water column is not restricted to just the volume of the moonpool, but a reasonable amount of water underneath the hull is dragged along with the water column, resulting in the added mass term a_h. As can be seen, two damping terms are present in the first line. b_h, which is a linear damping coefficient, is related to the ordinary hydrodynamic damping. The second term however, b_2 is a quadratic damping coefficient. This quadratic damping is due to vortex shedding near the inlet of the moonpool, as well as to friction between the wall of the moonpool and the water column. As the energy loss related to wave radiation from the moonpool is relatively small in comparison with the energy loss due to viscous effects, these quadratic terms are needed in order to fit model tests.
The second line in the equation describes the relation with the heave motion of the ship. As h describes the water motion relative to the ship, the moonpool is a coupled system. Therefore, the added mass, and damping of the moonpool should also be included in the ship-related part of the equation to describe this coupling (interaction coefficients d_{hz} & e_{hz}).

A similar, simplified equation is recommended by DNV [3]. Here, the absolute motion of the water plug (h_{abs} is considered.

$$\left(\rho A\left(H+\kappa\sqrt{A}\right)\right)\ddot{h}_{abs}+b_{eq}\left(\dot{h}_{abs}-\dot{z}\right)+\rho g A h_{abs}=F_{ext} \tag{3.2}$$

where

κ :Coefficient for considering increased draft $[-]$
h_{abs} :Absolute motion of the water in the moonpool $[m]$
b_{eq} :Equivalent linearized damping coefficient $[kg/s]$

In equation 3.2 the added mass is accounted for by $a_m = \rho A\kappa\sqrt{A}$ with κ an empirical coefficient depending on the shape of the moonpool. For rectangular moonpools this value is found to be in between 0.45 and 0.47, while circular shaped moonpools a value of 0.48 should be used. Additionally, the quadratic damping term has disappeared and both the linear and quadratic damping are replaced by a linearized equivalent damping coefficient (b_{eq}). This linearisation is conventional once frequency domain calculations are considered. Where time domain calculations are able to predict non-linear damping terms, frequency domain calculations require linear equations of motions. By taking into account this equivalent damping term should dissipate the same amount of energy during a certain interval, b_{eq} is derived as follows:

$$\frac{1}{T}\int_0^T \left(b_{eq}\dot{z}\right)\dot{z}dt = \frac{1}{T}\int_0^T \left(b_1\dot{z} + b_2\dot{z}|\dot{z}|\right)\dot{z}dt \tag{3.3}$$

where

T :Motion period $[s]$

Evaluating these integrals assuming $\dot{z}$ is a harmonic function of the form $\dot{z} = -z_a\omega sin(\omega t + \epsilon)$ leads to the following expression for b_{eq}:

$$b_{eq} = b_1 + \frac{8}{3\pi}\omega z_a b_2 \tag{3.4}$$

3.2. RESONANCE

As the moonpool acts as a single mass-spring system, dynamic amplification of the water motions in the moonpool can occur. This phenomenon is called resonance and could result in high relative motions in the moonpool, even though the exciting incoming wave is of a lower amplitude. As large motion amplitudes could cause significant loads on structures, as well as green water on deck, it is important to know for which conditions resonance can occur. A few studies describe the resonance conditions of the moonpool by means of moonpool dimensions and the hydrostatic stiffness.

3.2.1. MASS-SPRING SYSTEM

Following the fundamentals of a mass-spring system, Faltinsen [4] suggests the following equation for the resonance period of the moonpool:

$$T_n = 2\pi\sqrt{\frac{M}{k_{hyd}}} = 2\pi\sqrt{\frac{\rho AH}{\rho Ag}} = 2\pi\sqrt{\frac{H}{g}} \tag{3.5}$$

where

T_n :Natural period $[s]$
M :Total water mass in the moonpool $[kg]$
k_{hyd} :Hydrostatic stiffness $[\frac{N}{m}]$

In equation 3.5 added mass is not accounted for. However, in general the added mass takes up a significant part of the total mass moving in the moonpool. Therefore, DNV includes the earlier mentioned representation of the added mass. This yields:

$$T_n = 2\pi\sqrt{\frac{H + \kappa\sqrt{A}}{g}} \tag{3.6}$$

3.2.2. POTENTIAL THEORY

Molin [5] did an extensive study on the different mode shapes of rectangular moonpools and its natural periods. By means of potential theory he derived a similar expression for the first natural period of the moonpool, the piston mode. For this theory the assumption was made that the water depth is infinite and the dimensions of the ship are much larger than the moonpool. Solving the boundary value problem at the bottom of the moonpool, the expression for the natural period of the moonpool becomes

$$T_n = 2\pi\sqrt{\frac{H + Bf_3}{g}} \tag{3.7}$$

where

$$f_3 = \frac{1}{\pi}\left\{sinh^{-1}\left(\frac{L}{B}\right) + \frac{L}{B}sinh^{-1}\left(\frac{B}{L}\right) + \frac{1}{3}\left(\frac{B}{L} + \frac{L^2}{B^2}\right) - \frac{1}{3}\left(1 + \frac{L^2}{B^2}\right)\sqrt{\frac{B^2}{L^2} + 1}\right\} \tag{3.8}$$

For both equation 3.6 and 3.7 the governing parameter is the draft of the moonpool. How the draft is related to the natural period is shown in figure 3.2. Here the dimensions of the moonpool of DCV Aegir have been used. The draft is chosen to be 10.5 m, as this is the general draft used during operations:

Length [m]	Width [m]	Draft [m]

Table 3.1: Moonpool specifications

CONFIDENTIAL

Figure 3.2: Natural period of the moonpool of DCV Aegir

Using a value for κ of 0.46 the lines of both expressions for the natural period are lying close to each other. For the operational moonpool draft of m a natural period can be found of approximately seconds.

3.3. MODEL TESTS

3.3.1. SCALE MODEL

Prior to the construction of DCV Aegir, a scale model has been made to study the hydrodynamic characteristics of the vessel. Next to vessel motions, also the characteristics of the moonpool have been investigated for both operational and transit conditions. In a thesis conducted by Dilk [6] these model test have been analysed and validated by means of a Computational Fluid Dynamics (CFD) model. The most relevant tests for this study were the tests where the freely floating model is subject to a JONSWAP spectrum of a significant wave height $H_s = 4m$ and a peak period $T_p = 10s$ from different wave directions. During this test, the water motions in the moonpool were measured to determine the RAO of the moonpool. By taking the Fourier transform of the time-trace in the moonpool, the power spectral density of the water motions in the moonpool is obtained. Subsequently, the RAO of the moonpool is calculated by

$$RAO_{MP,rel\,\zeta} = \sqrt{\frac{S_{MP}}{S_\zeta}} \tag{3.9}$$

The resulting RAO's of the model tests are shown in figure 3.3. A strong amplification for each wave direction is observed at . This corresponds to a wave period of seconds. The moonpool is more prone to resonance in beam wave conditions than for quartering waves, 90° waves cause more excitation than waves coming from 270 °.

Figure 3.3: Moonpool RAO's from model tests for specific wave directions

3.3.2. CFD MODEL

An important parameter for the water motions in the moonpool is the damping. Resonance behaviour in the moonpool is a damping related phenomenon, which means that the amount of damping strongly influences the motions. Both the linear and quadratic coefficients from the equations of motion from section 3.1 can be determined by a so called decay test. For the determination of the damping coefficients for the roll and heave motions this is common practice, but the same principle can be applied to the moonpool. During a decay test, the motion of interest is given an initial displacement, after which it is decaying to a stable position. During this motion decay, energy is dissipated by means of damping. The rate of decay is dependent on the damping coefficients and can thus be determined.

As no waves and vessel motions are present in a decay test, the forcing equals to zero. This reduces equation of motion 3.1 to

$$(M + a_m)\,\ddot{h} + b_1 \dot{h} + b_2 \dot{h}\,|\dot{h}| + k_{hyd} h = 0 \tag{3.10}$$

Dividing this equation by $(M + a_m)$ gives

$$\ddot{h} = -p_1 \dot{h} - p_2 \dot{h}\,|\dot{h}| - \omega_0^2 h \tag{3.11}$$

where

$$p_1 = \frac{b_1}{M + a_m},\; p_2 = \frac{b_2}{M + a_m} \text{ and } \omega_0 = \sqrt{\frac{k_{hyd}}{M + a_m}}$$

Assuming the damping stays constant with respect to the amplitude of the motion, p_1 and p_2 can be found from the relation

$$\frac{2}{T_h} log\left(\frac{h_{n-2}}{h_{n+2}}\right) = p_1 + \frac{16}{3}\frac{h_n}{T_h} p_2 \tag{3.12}$$

T_h and h_n are defined in figure 3.4

As this decay test has not been carried out during the scale model campaign, it was chosen to be done by means of a CFD model test. Here the water in the moonpool was given an initial offset of 5 and 2.5 m. Assuming the velocity profile over the depth of the moonpool is constant for a constant moonpool area, the water velocity was measured at the inlet of the moonpool. By integrating the velocity, the displacement of the water was calculated. With the displacement and period of the oscillation known, the coefficient p_1 and p_2 were calculated using equation 3.12.

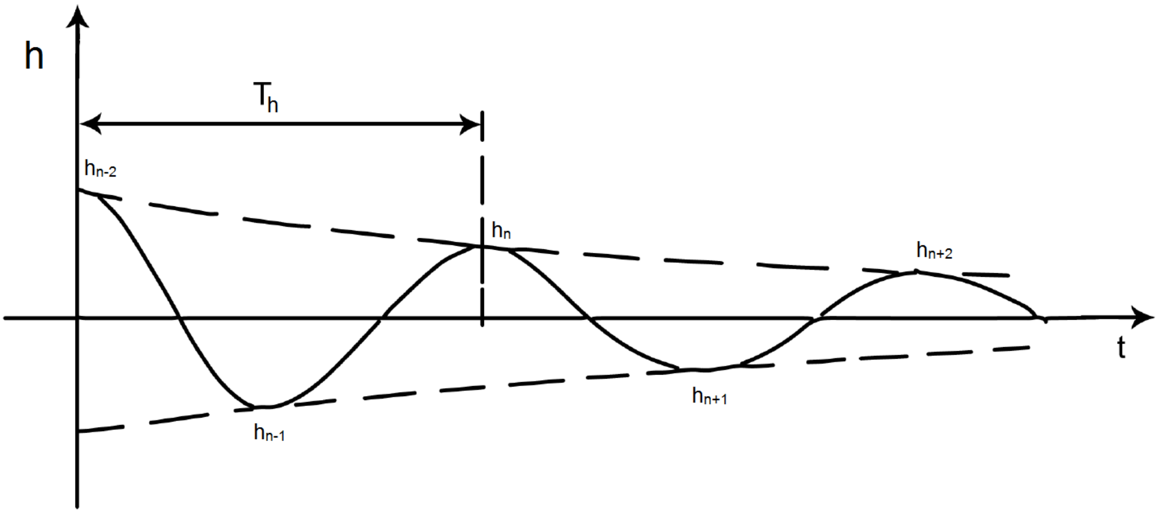

Figure 3.4: A typical decay test

3.4. STRUCTURES IN THE MOONPOOL

So far, only empty moonpools have been considered. However, for installation purposes it is of importance to know what effect structures in a moonpool have on the motions in the moonpool and what forces are related to these motions. Resulting from typical moonpool RAO's, for most sea states the wave energy is located outside of the range of the moonpool RAO peak. This means most of the incoming wave energy is filtered out and not amplified by the moonpool. Therefore, the moonpool has a sheltering function most of the time. However, for sea states containing a significant amount of energy around the resonance period of the moonpool, the water motions in the moonpool can get rather large. Until recently, it was assumed that structures in the moonpool only moderately alter the flow conditions of the moonpool. However, a recent study conducted at MARINTEK [7] shows that structures do change the fluid motions to a large extend. Due to additional viscous damping and friction, but also because of the water exerted force on the object, energy is dissipated from the water flow. This does not only decrease the amplitude of the motion significantly, but the oscillation period does also increase.

3.4.1. MORISON'S EQUATION

In 1950 Morison [8] released a paper in which he proposed an empirical equation to calculate the loads on fixed vertical piles subject to waves. This equation is a superposition of two load components; a quadratic drag term and a linear inertia term, yielding

$$F(t) = \rho C_M V_r \dot{u}(t) + \frac{1}{2}\rho C_D A_{body} u(t)\,|u(t)| \tag{3.13}$$

where

C_M :Inertia coefficient $(C_A + 1)$ $[-]$
C_A :Added mass coefficient $[-]$
V_r :Reference volume of the body $[m^3]$
C_D :Drag coefficient $[-]$
A_{body} :Cross-sectional area of the body $[m^2]$

As a structure hanging in the moonpool is either supported by the crane or by the J-lay tower, the structure is assumed to by fixed in the moonpool. Therefore Morison's equation as formulated in equation 3.13 is well suitable for calculating the loads on the structure. In order to calculate the loads on a structure in the moonpool, next to the water motions in the moonpool the drag and inertia coefficients should be known. These coefficients are determined by means of experiments for a wide variety of shapes and sizes. For the 18" ILT installation the structure considered is the weight compensation buoy, which dimensions are listed in table 3.2.

Buoy weight		Buoy dimensions		
In air [mT]	Submerged [mT]	Length [m]	Width [m]	Height [m]
100.7	-150	6.444	6.025 (top) 4.15 (bottom)	9.490

Table 3.2: Weight compensation buoy specifications

Det Norske Veritas (DNV) has listed [9] the hydrodynamic properties of several shapes. For box-like structures, the added mass coefficient is determined by starting with the assumption that the buoy is a flat plate with a shape resembling the projected surface perpendicular to the flow. In the case of the buoy this surface is the top surface, which is 6.444x6.025 m. However, the length of the structure does influence the flow characteristics and the volume of water dragged along with the structure. Therefore, for structures in heave, a 3D-correction factor is used to convert the added mass of a 2D plate to a 3D structure. This correction factor is defined in equation 3.14.

$$\alpha_{3D} = 1 + \sqrt{\frac{1-\lambda^2}{2\left(1+\lambda^2\right)}} \tag{3.14}$$

with

$$\lambda = \frac{\sqrt{A_p}}{L + \sqrt{A_p}} \tag{3.15}$$

where

α_{3D} :3D correction factor $[-]$
L :Longitudinal dimension of the object $[m]$
A_p :Projected area perpendicular to the flow $[m^2]$

Using the correction factor of the added mass of a 3D body, a new reference volume can be calculated. The reference volume for a 2-D plate is defined as

$$V_r = \frac{\pi}{4} a^2 b^2 \tag{3.16}$$

where a and b are defined as depicted in figure 3.5. Multiplying this 2D reference volume with α_{3D} the reference volume for the 3D object is obtained. As the reference volume is different from the volume of the body, the expression for the inertia coefficient ($C_M = 1 + C_A$) used in Morison's equation does not hold anymore. Splitting the inertia part in a structural mass and an added mass part, Morison's equation becomes

$$F(t) = \left[\rho C_A V_r + \rho V_{body}\right] \dot{u}(t) + \frac{1}{2} \rho C_D A_{body} u(t)\,|u(t)| \tag{3.17}$$

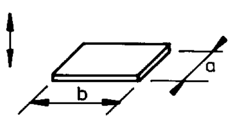

Figure 3.5: 2D plate definition

b/a	C_A
1.00	0.579
1.25	0.642
1.50	0.690
1.59	0.704
2.00	0.757
2.50	0.801

Table 3.3: b/a ratio with corresponding C_a values

As stated, C_A is dependent of the dimensions of the projected area of the buoy. This area corresponds to the top area of the buoy for vertical loading. Using these values to interpolate for C_A in table 3.3 yields an added mass coefficient of 0.596.
The drag coefficient in Morison's equation accounts for the force encountered by the structure due to an overpressure at the front of the structure and an underpressure at the back of the structure. This pressure

difference is caused by disturbance of the fluid flow. Water tends to flow more easily around an aerodynamic structure than for example a flat plate. Therefore, a flat plate will have a higher drag coefficient. Not only does the shape of the structure influence the drag coefficient, also the flow velocity and character influences the drag coefficient to a large extend. Drag coefficients in an oscillatory flow for example could get up to 3 times higher than those in a steady flow.

Due to the complex character of the drag coefficient, it is difficult to give a general formulation for the coefficient for complex shaped structures. Coefficients can be determined by means of experiments or an extensive CFD study. If no experimental or CFD data is available however, DNV suggests to use a C_D value for structures in oscillatory flows of 2.5.

3.4.2. MOONPOOL INFLUENCE

The hydrodynamic properties of the buoyancy module found in section 3.4.1 were based on unconfined oscillatory flow conditions. However, as the structure is subject to water motions in the moonpool, this assumption does not hold. The flow is confined by the walls of the moonpool and does therefore behave different. Not only are the hydrodynamic coefficients dependent of the shape of the structure, but also the boundaries of the flow influence the hydrodynamic properties. In general, if the flow around an object is restricted, the hydrodynamic forces on the structure increases. In order to account for this increase, DNV suggests and alteration of the hydrodynamic coefficients based on the so called blockage factor of the structure [3]. This blockage factor is the percentage of moonpool area blocked by the structure. In the case of the buoyancy module of the 18" ILT installations this blockage factor is approximately . The blockage factor is incorporated by

$$\frac{C_D}{C_{D0}} = \frac{1 - 0.5 A_{body}/A}{\left(1 - A_{body}/A\right)^2} \qquad \text{for } A_{body}/A < 0.8 \tag{3.18}$$

$$\frac{C_A}{C_{A0}} = 1 + 1.9\left(\frac{A_{body}}{A}\right)^{\frac{9}{4}} \qquad \text{for } A_{body}/A < 0.8 \tag{3.19}$$

where

C_{D0} :Drag coefficient for unrestricted flow $[-]$
C_{A0} :Added mass coefficient for unrestricted flow $[-]$
A_{body}/A :Moonpool blockage factor $[-]$

Substituting the previously found coefficients C_{D0} and C_{A0} for the buoyancy module into equations 3.18 and 3.19, the hydrodynamic coefficients for the restricted flow become $C_D =$ and $C_A =$.

3.4.3. INERTIA & DRAG DOMINANCE

Following from section 3.4.1, the added mass coefficient can be well approximated. However, the drag coefficient should be obtained by means of experiments or CFD studies in order to get realistic values. Additionally, frequency domain calculations, to determine the motions of the moonpool from a force time-trace, can not be solved due to the quadratic (non-linear) character of the drag term. Therefore, it is favourable to know whether the system is drag or inertia dominated. To do so, the so-called Keuligan-Carpenter (KC) number can be used to get an indication of the behaviour of the system. The KC number yields

$$KC = \frac{u_a T}{D} \tag{3.20}$$

where

KC :Keuligan-Carpenter number $[-]$
u_a :Water velocity amplitude $[\frac{m}{s}]$
D :Characteristic diameter $[m]$
T :Water motion period $[m]$

The dimensionless number KC depends on the amplitude multiplied by the water motion period divided by a characteristic diameter. For circular objects this is indeed the diameter, but for different shaped objects, like the buoy, this is the projected width. According to Journee [1], low KC numbers inertia dominates, while for high KC numbers the drag is governing. Taking a conservative wave height in the moonpool of 4 m with a period of 8.3 seconds, the maximum velocity amplitude is $1.5\frac{m}{s}$. Together with the smallest width of the buoy, 6.025 m, the KC number for the buoy in the moonpool is approximately 2.1. As can be seen from table 3.4, this is well within the limits of inertia dominance, and thus it can be concluded that the situation that a large buoy is hanging in the moonpool is inertia dominated. Consequently, the drag term can be neglected for this case.

KC value	Dominance
<3	Inertia dominant. Drag neglected.
3 - 15	Inertia + linearized drag
15 - 45	Full Morison
>45	Drag dominant. Inertia neglected.

Table 3.4: KC values with corresponding dominance

3.4.4. STRUCTURE INFLUENCE

Generally, it is assumed that structures do not influence the resonance behaviour of water in the moonpool as the resonance period is dominantly influenced by the draft of the vessel. Therefore, practice is to calculate hydrodynamic loads on structures using empty moonpool conditions. However, recent research of Aspelund at Marintek [7] shows significant changes in both the motion amplitude, as well as in the natural period of the moonpool when an object is introduced. In section 3.2 the analytical expressions for the moonpool resonance period are given. These include the classic description of the resonance period of a simple mass-spring system. However, in fundamental dynamics the resonance frequency of an underdamped system is given by

$$\omega_r = \omega_0\sqrt{1-2\zeta^2} \tag{3.21}$$

where

ω_r :Resonance frequency $[Hz]$
ω_0 :Undamped natural frequency $[Hz]$
ζ :Damping ratio $[-]$

As an object in the moonpool introduces damping in the moonpool, not only the amplitude of the water motions is reduced, but according to eq. 3.21 the resonance period also shifts towards a longer period. Consequently, moonpool RAO's also shift and decrease in amplitude. This effect is observed in the resulting RAO's of Aspelund's research in figure 3.6.

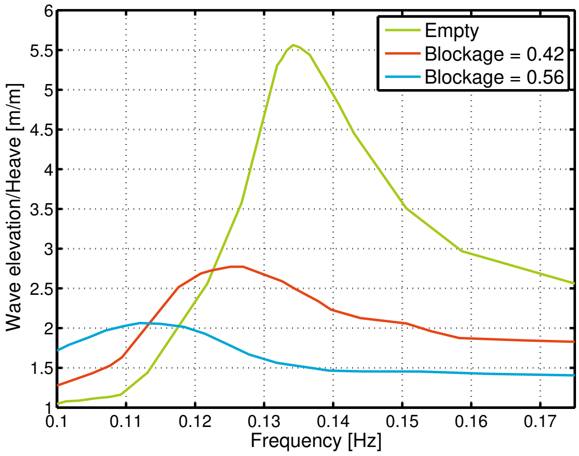

Figure 3.6: Influence of objects in a moonpool on the moonpool RAO

4

Moonpool measurements

Although the literature does describe the principles behind water motions in the moonpool, there is much room for interpretation. In order to make realistic calculations of the DCV Aegir moonpool, realistic values should be obtained. DCV Aegir is one of the newest pipe-lay vessels in the industry and equipped with load measurement sensors in the J-lay tower, but also the water motions in the moonpool are continuously monitored. In this chapter, these water motions in the moonpool are analysed and compared with the measured waves outside of the vessel to determine the response behaviour of the water in the moonpool. As a verification, diffraction software is used to validate the found relations.

4.1. Wave motions

During the Ichthys project, the external waves have been measured, as well as the water motions in the moonpool. The sensor recording these moonpool water motions is located beneath the work station, and is, consequently, moving with the ship. The measured motions in the moonpool are therefore motions relative to the ship. As the ILT-weight-compensation buoy is assumed to also move with the ship, the loads induced by the relative wave motions around the buoy are the same as those measured by this sensor. The external waves are being measured by a wave rider buoy employed close to DCV Aegir and is generating a wave spectrum every hour.

4.1.1. Incoming waves

The external waves are measured by a wave rider buoy which is capable of measuring not only the wave height and period, but also the direction of the different wave components. Every hour this data is combined into a direction wave spectrum and stored in the measurement system. This directional wave spectrum can be depicted as a polar plot as shown in figure 4.1a or in a 1D plot with an extra line representing the governing wave direction for each frequency component (figure 4.1b).

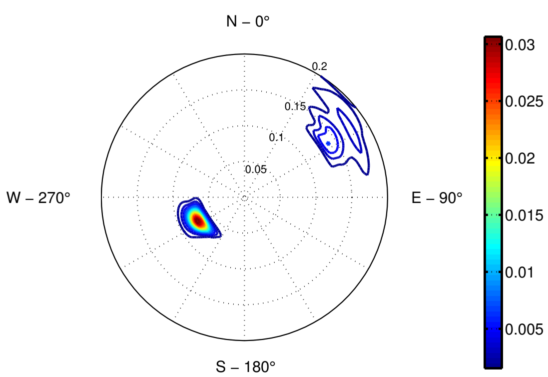

(a) Global directional wave-spectrum

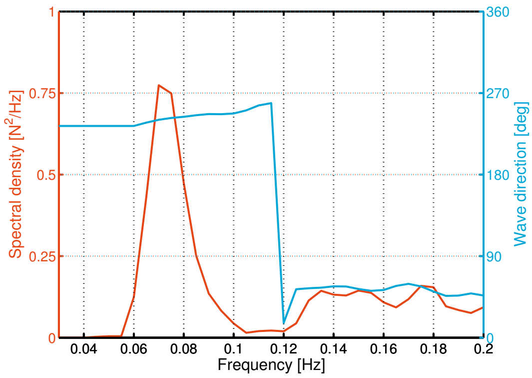

(b) 1D wave spectrum

Figure 4.1: Incoming wave-spectrum

Figure 4.1a and figure 4.1b both represent the same seastate measured during one hour. Two clear wave partitions, coming from different directions, can be distinguished from these graphs; a sharp peak caused by the swell waves coming from a 240° direction and more spreaded wind wave component coming from a 60° direction. During the Ichthys project this swell peak is often observed from this particular direction. The wind sea however is generated by local weather disturbances and is not related to one particular wave direction.

4.1.2. MOONPOOL WATER MOTIONS

The sensor measuring the water motions in the moonpool uses radar technology to measure the wave motions in the moonpool. As the wave elevation in the moonpool is measured 5 times per second, a high resolution time trace is generated continuously. Using a discrete Fourier transform, the different frequency components can be calculated resulting in a spectral density graph. A sample of this time trace and the corresponding spectral density plot is depicted in figure 4.2.

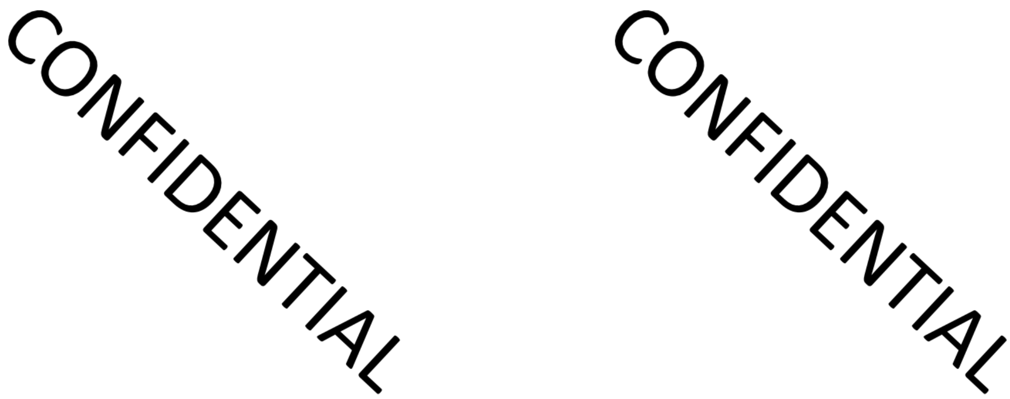

(a) Moonpool timetrace (b) Spectral density moonpool

Figure 4.2: Moonpool measurements

In the spectral density plot generated from the time trace a sharp peak is observed. This peak is in correspondence with the assumption that the moonpool of DCV Aegir is only excited by waves around it's natural period.

4.2. MOONPOOL RAO'S

In order to describe the relation between the motion behaviour of a vessel and the incoming waves, RAO's are used. This relation has earlier been defined by equation 2.1. In order to describe the relation between incoming waves and the water motions in the moonpool a similar approach can be used. Instead of vessel motions now the water motions of the moonpool are utilized to calculate an RAO. As both a spectrum for the incoming waves and a spectrum for the moonpool motions are available, the RAO for the relative wave height in the moonpool can be described by eq. 3.9. Inserting two arbitrary spectra of the incoming waves and the moonpool motions (figure 4.3a) into eq. 3.9 results in the RAO depicted in figure 4.3b. A strong amplification of the frequencies around the moonpool natural frequencies is evident from this graph. However, just outside the resonance period of the moonpool, incoming wave energy is filtered out and not let through in the moonpool. As this RAO is related to a wave spectrum with swell and wind seas coming from a certain direction, it does not necessarily mean that for different wave components and wave directions, a similar RAO would be obtained.

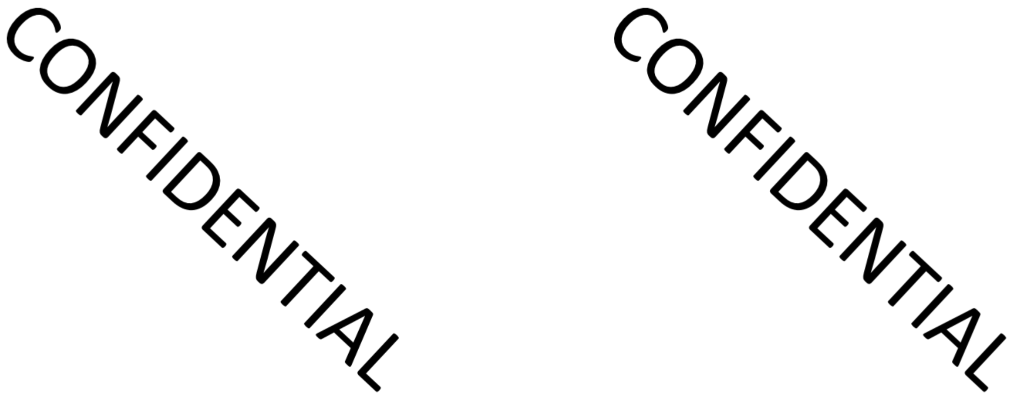

(a) Wave and moonpool specrum

(b) Moonpool relative wave height RAO

Figure 4.3: Moonpool RAO

In order to get a more solid insight concerning the influence of the wave direction, RAO's have been developed for every hour of measurements during Ichthys, resulting in approximately 8000 RAO's. The calculations and scripts used to get to these RAO's is elaborated in appendix A. By sorting the calculated RAO's per wave direction and taking into account the heading of DCV Aegir, RAO's for wave directions relative to DCV Aegir are obtained. As can be seen from figure 4.4a this still results in a rather wide band of RAO's. Therefore the 90% non-exceedance value (black line) has been chosen to represent the RAO's shown in the polar plot of figure 4.4. Here the 0° represents waves coming from the aft of the ship and 180° are head waves. Consequently, 90° and 270° are beam waves. On the radial axes, the wave frequency is shown, while on the angular axes the wave direction is depicted.

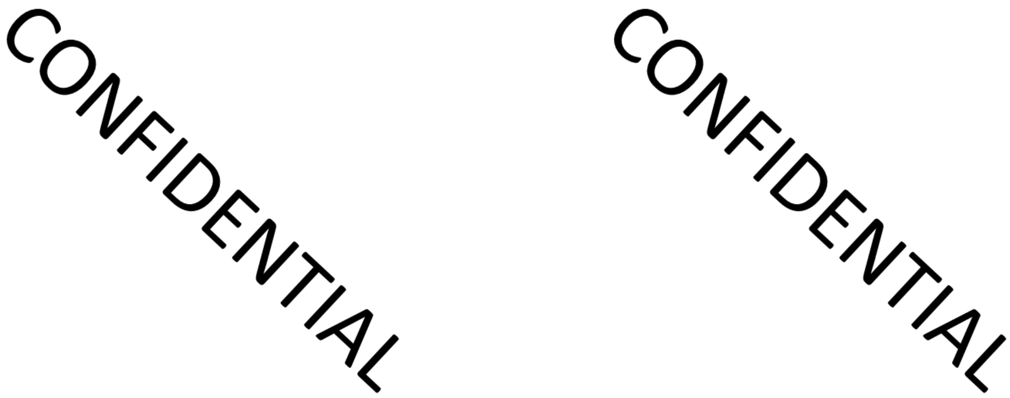

(a) Moonpool RAO's for 0 ° waves

(b) Moonpool RAO's for all wave directions

Figure 4.4: Direction dependent moonpool RAO's

Similar to the results obtained for a single RAO a strong amplification is found around , the resonance frequency of the moonpool. This frequency is similar for each wave heading according to the polar plot. However, the magnitude of the RAO is clearly dependent on the incoming wave heading. Close-to-beam waves seem to cause the most severe excitation, while head waves are the lowest. Also for aft waves the excitation is lower than for beam waves.

4.3. VISCOUS DAMPING

Using an RAO to describe the response of the moonpool on incoming waves assumes that the water motions in the moonpool are proportional to the incoming wave height. The water motions in the moonpool are governed by wave induced pressure at the location of the moonpool. This pressure is proportional to the incoming wave height. However, water motions in the moonpool are also influenced by viscous damping induced by vortices shed by the moonpool wall and inlet [7]. The amount of vortices shed is dependent on the velocity of the water, which means that for larger particle velocities in the moonpool, the viscous damping increases. This yields a non-linearity in the relation between incoming waves and water motions in the moonpool. For larger incoming wave heights, the water in the moonpool should respond less than for small incoming wave heights. In order to show this phenomenon, the RAO's determined in the previous section are not only sorted by wave direction, but also by the incoming wave height. It should be noted that this wave height is based on either the swell peak or the wind wave peak, depending on which peak is in the region of the resonance period of the moonpool. Therefore, only a part of the wave spectrum's energy is used to determine the significant wave height. The results of this sorting is shown in figure 4.5.

CONFIDENTIAL

Figure 4.5: Wave height dependency of the moonpool RAO

A clear decrease in RAO magnitude is observed when the incoming wave height is increased. This is in accordance with earlier statements about the non-linear behaviour of viscous damping induced by the walls and inlet of the moonpool. Furthermore it can be seen that for larger significant wave heights the line becomes more peaky and irregular. This is due to the fact that higher sea states are encountered less frequently than the lower sea states. The wide band of RAO's shown in in figure 4.4a is also the result of the wave height related magnitude.

4.4. WAVE HEADING DEPENDENCY

From the directional RAO spectrum a second interesting phenomenon is found. The clear difference between the moonpool response on waves coming from the bow/aft direction of the ship and those coming from the beam direction. A good explanation for this observation has not been given in earlier research and should be looked at. In order to do this, the DCV Aegir is modelled and analysed by the use of the diffraction software package WAMIT. Diffraction software has proven to be accurate in predicting the resonance behaviour of the moonpool. However, potential theory does not account for viscous damping, which causes an overestimation of the moonpool excitation. This approach is therefore not suitable for obtaining realistic results concerning the magnitude. Nonetheless, the viscous damping is not wave direction dependent, so the (overestimated) results from WAMIT can be used to compare the difference in excitation for different wave directions qualitatively.

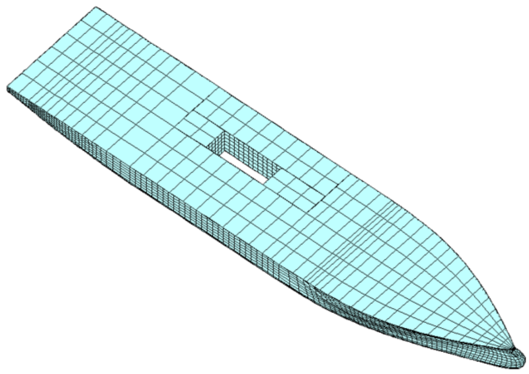

Figure 4.6: Panel model of the DCV Aegir

WAMIT is a software package that uses linear and second-order potential flow theory to calculate the interaction between waves and floating bodies. In order to do so, it solves the velocity potential and fluid pressure in these bodies by means of the boundary integral equation method (BIEM). This calculation is done with regular waves and per wave heading and should therefore be carried out for the whole frequency range of waves and all wave directions. In figure 4.6 the panel model of the DCV Aegir is shown. Only the submerged part of the vessel is modelled, as the emerged part of the vessel is not taken into account in the calculations. The wave frequencies being used range from 0.6 to 0.11 Hz for each wave direction. As earlier stated, the water motions in the moonpool of the DCV Aegir are solely dependent on the incoming waves and are not influenced by any of the vessel motions. Therefore, in order to reduce the simulation time, the Aegir is fixed in space and will not be moving with the waves. The results of the WAMIT calculations are depicted in figure 4.7 in a similar manner as done with the moonpool measurements of the DCV Aegir (figure 4.4).

CONFIDENTIAL

Figure 4.7: Moonpool response for every direction from WAMIT

A similar pattern as in the measurements is observed concerning the directional dependence of the excitation of the moonpool. This consolidates the observations of the measurements, but does not yet explain why this relation is present. To acquire more insight in this observation, a length-sensitivity study has been done using WAMIT. Several barges with a fixed width of 48 m, a draft of and a length varying from 48 to 360 m have been modelled. Each of these barges have a moonpool on midship with constant dimensions of 12x12 m. By imposing beam and head waves with a period of seconds, the resonance period of this specific moonpool, the relation between the length of the vessel and the response of the moonpool was investigated. Important to notice is that the wave used by WAMIT is a 1 meter wave. The response of the moonpool is therefore also directly it's RAO, as the RAO is defined as $RAO = \frac{x}{\zeta_a}$. The two barge models in figure 4.8 correspond to the 48 m and the 360 m barge respectively.

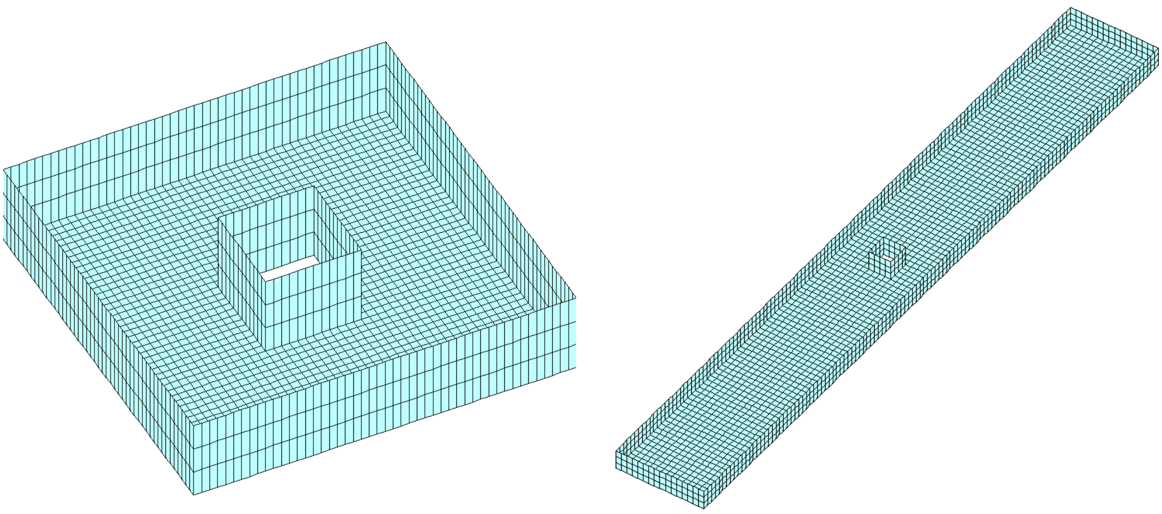

(a) 48x48 m barge model

(b) 360x48 m barge model

Figure 4.8: WAMIT barge models

If the response of the moonpool would be purely dependent on the distance between the wall of the moonpool and the wall of the barge, only the responses for head waves would differ. As the barge width stays constant, the RAO for each barge would be the same. However, the results of the WAMIT simulations show a different result. To show the effect of the barge length, the RAO's of several barges are depicted in one plot. This has been done for both beam and head waves in figure 4.9. For head waves, the RAO decreases for an increasing barge length. A more interesting observations however, is that for beam waves the RAO's are increasing for longer barge length. Clearly, not only the distance between the moonpool wall and the side of the ship is influencing the excitation of the moonpool.

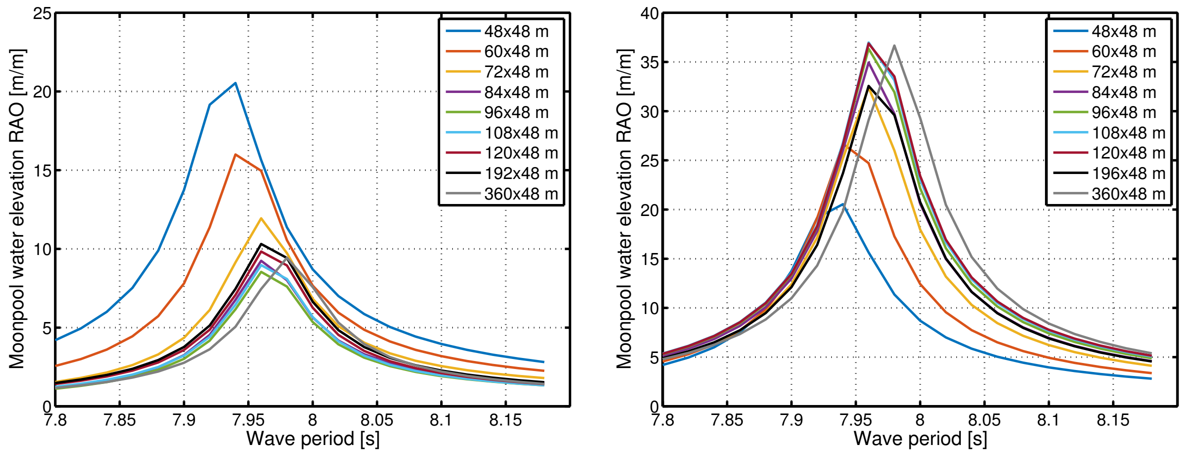

(a) RAO's for head waves

(b) RAO's for beam waves

Figure 4.9: RAO's for WAMIT barge models

Next to increasing RAO peaks for beam waves and decreasing peaks for head waves, the change in RAO tends to go to a certain limit. The differences in RAO's for barges ranging from 48 to 96 meter are rather significant, while a further increase in length does not seem to have a large influence on the RAO anymore. This counts for both head and beam waves. In order to understand this phenomenon, it is necessary to look at the excitation mechanism. From literature it is know that the excitation of the moonpool is governed by the hull pressure at the location of the moonpool. Therefor, cross-sectional displays of the pressures around the moonpool have been generated as well as the numerical output of the pressure. As earlier stated, due to the absence of viscous damping in potential flow theory, the response in resonance conditions tends to be overestimated. Accordingly, the resulting pressure around the moonpool will also be overestimated. To investigate why there is more response for certain lengths, the moonpool is closed off, so that the hull pressure at the location of the moonpool is purely the moonpool-wave exciting pressure. The wave period that causes resonant water motions in the moonpool is applied to the barge with the closed moonpool. From figure 4.9 can be found this wave period is approximately 8 seconds, which corresponds to a wave length of approximately 100 m. In figure 4.10 and 4.11 the free surface elevation and a cross-sectional profile of the hull pressure are shown for beam and head waves of a 96 m long barge respectively. Here the blue square represents the barge. Similar figures are available for barges of different lengths. These graphs can be found in Appendix B.

In figure 4.10 and 4.11 there is a clear pressure build-up at the side of the incoming wave. This pressure causes a significant part of the incoming wave to be reflected, which is clearly visible in the standing wave pattern in front of the incoming wave side. A smaller part is diffracted at the edges and bending around the barge. Still, only little wave energy is getting behind the barge, which causes a wave shadow zone. This observation is similar to the effect seen with detached breakwaters. The remaining part of the incoming wave is the part which is moving underneath the barge to the other side. This is the result of a pressure difference between the two sides of the barge. It is this pressure that also causes the excitation of the water in the moonpool. As can be seen in the bottom graphs of figure 4.11 the pressure decreases exponentially from the hull side (red lines) towards the lee side. Accordingly, as the moonpool is excited by hull pressure fluctuations, the moonpool response is directly related to the distance between the ship wall and the moonpool. Although this distance is kept the same for the barge models, the response differs for different barge lengths. In order to

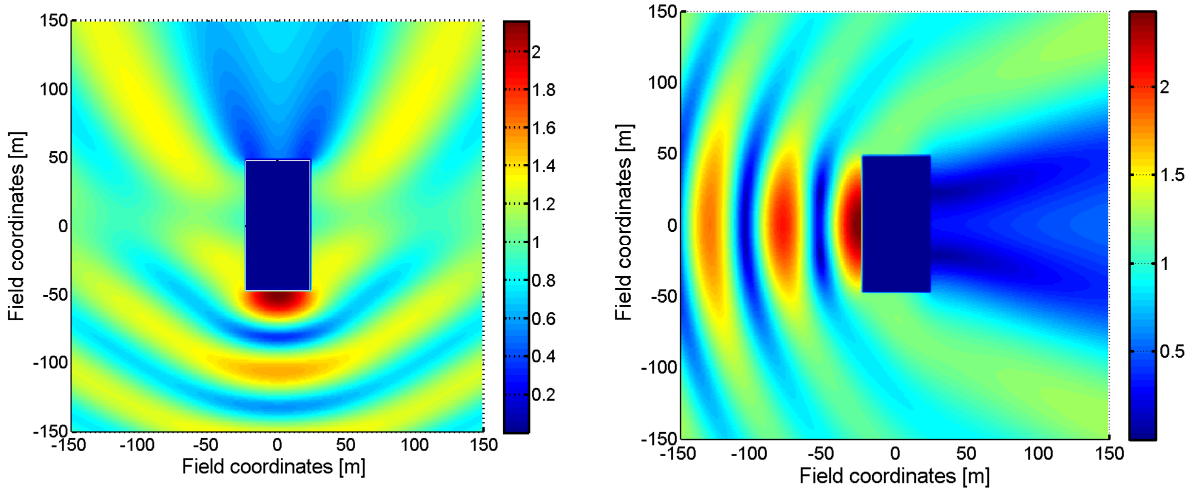

(a) Head waves (b) Beam waves

Figure 4.10: Surface elevation for 96 m long barge

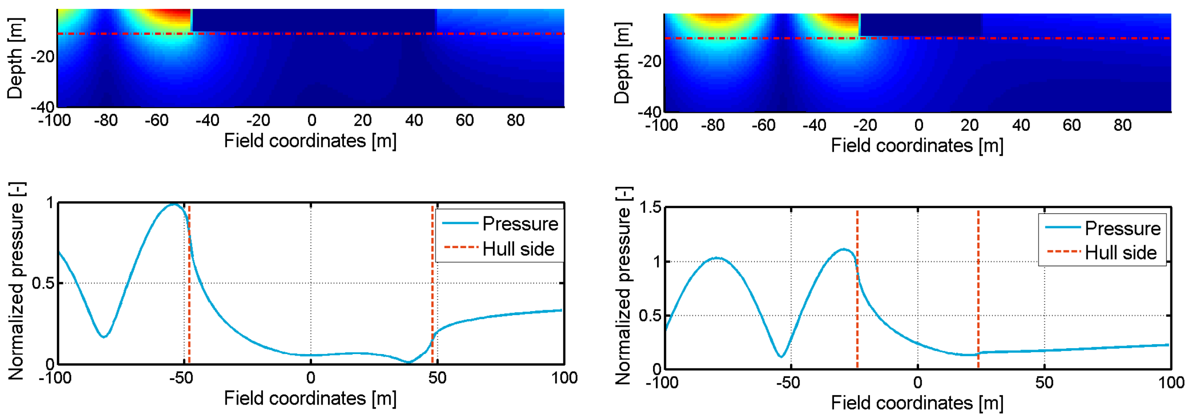

(a) Head waves (b) Beam waves

Figure 4.11: Hull pressure distribution for 96 m long barge

get a better insight in the relation between the length of the barge and the water motions in the moonpool, in figure 4.12 the wave induced hull pressure at the location of the moonpool is plotted against the barge length.

In correspondence with what is earlier observed concerning the change in RAO's for the water motions in the moonpool, there is a clear pressure increase for beam waves and a similar pressure decrease for head waves. However, the RAO's shown in figure 4.9 have only been developed with a small length increments up to 120 m length. In figure 4.12 the small increments extend up to 408 m, which reveals a remarkable relation. For beam waves, the pressure indeed increases steadily up to a barge length of 120 m. This is due to the fact that up to that length, it is increasingly harder for the waves/pressure to move around the barge. For barge lengths more than 120 m the pressure underneath the barge starts to fluctuate. While this is a significant fluctuation for beam waves, the pressure induced by head waves does not seem to change significantly for barge lengths larger than 120 m. To explain this phenomenon, a case with a maximum pressure (120 m length) will be compared to a case with a pressure low (192 m). In figure 4.13 the free surface elevation for these two cases are set side to side. Although there is not a clear difference in wave pattern at the lee-side of the barge, there is remarkable difference between the pressure build-up at the 120 m barge and the 192 m barge. Where the 120 m barge shows one particular area of maximum pressure at the middle of the barge - the location of the moonpool -, the pressure field along the length of the 192 m barge shows two pressure maximums, with a gap in between. Consequently, the pressure underneath the barge at the location of the moonpool is also lower.

The wave reflection pattern observed in figure 4.13 is due to interference of the diffracted waves generated

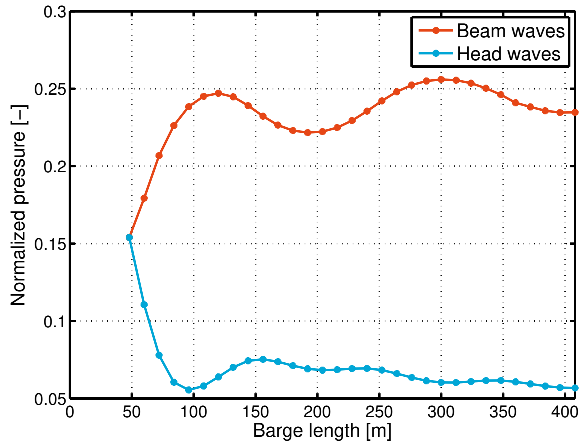

Figure 4.12: Hull pressure at moonpool location against barge length

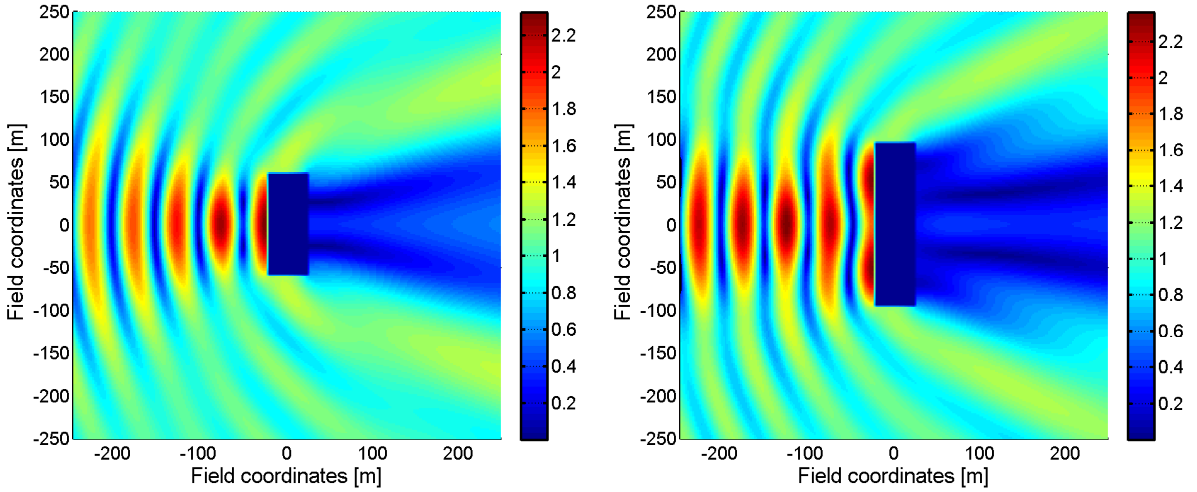

(a) 120 m barge

(b) 192 m barge

Figure 4.13: Surface elevation comparison between a 120 and 192 m barge ($T_p = 8s$)

at the boundaries of the barges. They occur at barge lengths approximating the incoming wave length or a multiple of the wave length. Similar patterns are observed at the incoming wave side of detached breakwaters [10] [11]. However, as breakwater literature is mainly focussing on the wave shadow zone behind the breakwater, the pattern has not been described yet. In this case the incoming wave length is approximately 100 m, which multiples correspond to the maxima and minima of figure 4.12. This yields the following relation between maximum pressure at the centre of the barge and the length of the barge:

$$L_{max\ press} = n \cdot \lambda \quad \text{with n = 1,3,5...} \tag{4.1}$$

From these observations we can draw the following statements concerning the wave induced pressure underneath the hull related to the barge length:

1. For hull lengths up to the incoming wave length, the pressure increases as the hull length increases.
2. For hull lengths larger than the incoming wave length, interference occurs and the hull pressure splits into multiple pressure maxima which are related to multiples of the wave length.

As the natural period of the moonpool of the DCV Aegir is seconds, which corresponds to a wave length of m, a similar pattern is expected as the length of the Aegir is m . In figure 4.14 the surface elevation graph of the Aegir is shown. It can be seen that at the rear half of the Aegir there is a pressure build-up. This is due to the earlier described phenomenon related to the wave length. At the front part of the Aegir, there is a slight increase in pressure, although this is reduced by the changing hull shape. The moonpool is marked by a white square, and as can be seen, the moonpool is located just beneath the centre of the hull, towards the part with the higher pressure. In this case, the formation of a pressure maximum at the rear of the Aegir is increasing the excitation of water motions in the moonpool.

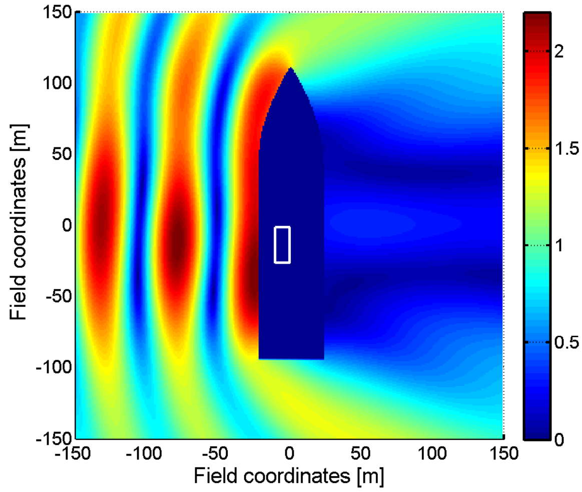

Figure 4.14: Surface elevation for the Aegir subject to beam waves ($T_p = s$)

In general, the distance between the side of the ship and the moonpool is the governing parameter for motion excitation. The observed local pressure maxima could however influence this excitation if the moonpool is located close to the side of the ship. This phenomenon is showed in figure 4.15 with the location of the moonpool in the longitudinal direction represented by the red dotted line. DCV Aegir has the centre of the moonpool located 18 meter from the hull wall. According to the blue line in the figure, the pressure does not change much over the length of the ship for that distance. Thus, the interference effect is irrelevant for the DCV Aegir. Would the moonpool have been located closer to the side, this effect would have influenced the response of the moonpool though.

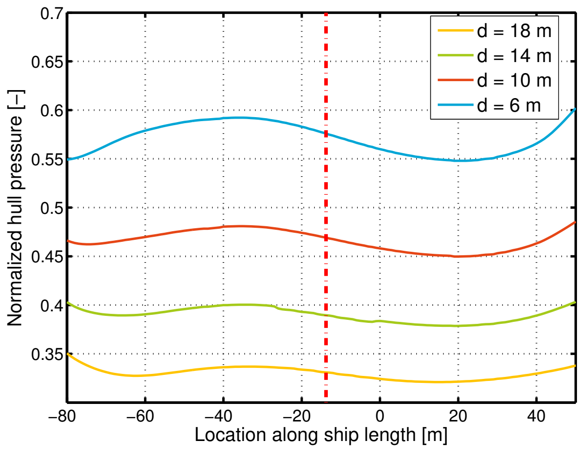

Figure 4.15: Hull pressure over the length of the ship with d the distance to the ship side

4.5. STRUCTURE EFFECT

So far the moonpool measurements considered in previous sections were for empty moonpool conditions. However, as described in chapter 3 the dynamic behaviour of the moonpool is changed once objects are introduced in the moonpool. During the pipe-lay campaign of the Ichthys project, most of the time only a pipe was present in the moonpool. Nonetheless, a reasonable amount of structures, like the 18" ILT's, have been installed through the moonpool. The weight compensation buoy involved in these installation blocks a substantial part of the moonpool when hanging in the moonpool, and expectedly changes the behaviour of the water motion. The down-looking wave radar measuring the water elevation in the moonpool is attached to the welding station, which most of the time is skidded away when large structures are lowered through the moonpool. Consequently, during most of the large structure installations measurements are not available. A few measurements have succeeded though and can be used to compare the behaviour between the empty moonpool and the case that a buoy is present. At a certain stage, the buoy is connected to the ILT and lowered through the moonpool. Once the buoy is completely submerged, the down-looking radar is able to measure the water motions in the moonpool again. From that point on, the travelling block is slowly moving down, taking the buoy down underneath the hull. During this installation step, the conditions in the moonpool are gradually changing to empty moonpool conditions. In order to show the effect of a buoy hanging in the moonpool, spectral density plots have been generated for the start and the end of this installation step (figure 4.16). The total duration of this phase is approximately 1 hour. Assuming the incoming sea state stays more or less constant during this hour, the change in spectral density of the moonpool water motions is purely related to the buoy.

Figure 4.16: Spectral density comparison between empty and non-empty moonpool conditions

What can clearly be seen, is that during the lowering of the buoy out of the moonpool, more wave energy is present in the moonpool. As explained by Aspelund [12], introducing objects in a moonpool yields a significant increase in viscous damping. Therefore, after removing the buoy from the moonpool, less energy is dissipated. A second effect of objects in the moonpool is a shift in natural period of the water in the moonpool. In experiments conducted by Aspelund, this effect is shown and from figure 4.16 a similar shift can be seen. The peak period shifts from seconds to the empty moonpool resonance period, seconds.

The particular shift in resonance period is explained by the extensive form of equation 3.6. The compact equation only accounts for moonpool with a constant area over the draft of the moonpool. However, in this case the buoy blocks off a part of the moonpool inlet, reducing the hydrostatic stiffness of the system. To account for this effect, the equation for the natural period of the moonpool yields

$$T_n = \frac{2\pi}{\sqrt{g}}\sqrt{\int_{-H}^{0}\frac{A(0)}{A(z)}dz + \frac{A(0)}{A(-H)}\kappa\sqrt{A(-H)}} \tag{4.2}$$

Here A(0) represents the moonpool area at the free water surface, and A(-H) the inlet area of the moonpool. Taking $A(0) = m^2$ and $A(-H) = m^2$, corresponding to a blockage factor of 0.16, the natural period of the moonpool shifts from to seconds (and Hz respectively). Although slightly higher than the measured period, the shift range is similar to what is observed in the measurement.

5

Model enhancement

Using the acquired knowledge from chapter 3 and 4 , the analysis procedure for structure installations through a moonpool can now be enhanced. In the original Flexcom model, the different water motions in the moonpool had not been accounted for. However, following from chapter 3 and 4, the behaviour of the moonpool is critical in the correct prediction of the loads. Two model enhancement procedures are proposed and validated by means of comparing the calculated loads in Flexcom with offshore load measurements. The validation shows that both the enhancement proposals are able to calculate realistic loads compared to the measurements. Finally, the new model proposals are applied on the original load case where the buoy and ILT are connected to both the crane and the travelling block.

5.1. Moonpool implementation

The main focus of Flexcom is the prediction of stresses and strains in a structural model of the installation and operational phase of a pipeline. The boundary conditions of a model are given as earth-fixed boundaries by means of static coordinates, such as an anchor point, or by moving boundaries, such as a ship. The latter is often defined as a set of points moving with respect to the COG of the vessel. The coupling between these motions and the encountered waves is given by a set of RAO's. As the RAO's of a vessel are well defined by model tests and diffraction software, Flexcom can predict the vessel motion reasonably well. However, diffraction is not taken into account by Flexcom, which means that the waves are not disturbed by the presence of the vessel. The real water motions in the moonpool are in fact the result of pressure differences caused by the diffracted incoming wave and vessel motions. Therefore the water motions in the moonpool should be defined separately. Two major differences between the incoming wave field and the moonpool water motions are governing:

1. **Piston mode**: Instead of the orbital water motions of the incoming wave field, the water motions are restricted to the vertical direction. As purely vertical wave motions cannot be implemented in Flexcom, a workaround has to be found to mimic the vertical motions.
2. **Energy reduction**: The moonpool acts as a filter. Only the wave energy around the moonpool resonance period is adding to the water motions in the moonpool. Therefore, a separate wave spectrum at the location of the moonpool should be included.

5.1.1. Model 1: Empty moonpool conditions

A first proposal of an analysis model for structure installations through a moonpool is based on the assumption that the water motion in the moonpool is not affected by the structure. In chapter 4 it is shown that the motions in the moonpool can be well described by reducing the incoming wave field by the use of an RAO. The RAO's for the relative water motion in the moonpool have been derived for each wave direction. General sea sates often consist of a wind and a swell related energy peak in the system, which not necessarily have the same direction. As the RAO's are only related to one particular direction, the direction of the peak with the most energy around the moonpool resonance period has to be used. 8.3 seconds, the resonance period of the moonpool of DCV Aegir is rather long for wind related waves, so in general the direction of the swell peak is to be used. Note that this wave direction is the wave direction with respect to the heading of the vessel.

Flexcom does not have the option to assign different wave spectra to separate domains of the model. The vessel motions are related to the undisturbed incoming wave and the structure loads are related to the moonpool water motions. To include both spectra in the analysis, the analysis is split into four parts:

1. The first part of the analysis yields the static analysis. During this step, the system is only subjected to gravitation and hydrostatic loads. The initial configuration is a guess of the static equilibrium of the system, but is not entirely stable yet. Therefore Flexcom calculates the real equilibrium. Once the solution is found, the simulation is stopped.

2. The second part of the analysis is semi-static. A static current load is imposed on the system configuration found in step 1. Once again, a static equilibrium is sought for by Flexcom, but now current loads are also affecting the system. As current cannot flow through the moonpool, the hydrodynamic coefficients of structures in the moonpool should be set to zero to exclude horizontal loads on these structures.

3. In the third part of the analysis, the system is dynamically loaded by waves . By setting the hydrodynamic coefficient of the structures in the moonpool to zero again, only the vessel is excited. The vessel motions are predicted by the vessel's RAO's and stored in a time trace for later use.

4. The last part of the simulation consists of calculating the loads on the structure in the moonpool. During this step, the vessel motions are given by the time-trace calculated in the previous step. Instead of the undisturbed wave spectrum, the incoming waves are now defined by the moonpool spectrum. Since the vessel motions are defined separately, only the structure in the moonpool is now affected by the wave motions. To account for the vertical motions of the moonpool, only the hydrodynamic coefficients of the structure in the horizontal plane are set to zero. As a result, the structure is only excited by the vertical component of the wave motions, mimicking the moonpool behaviour.

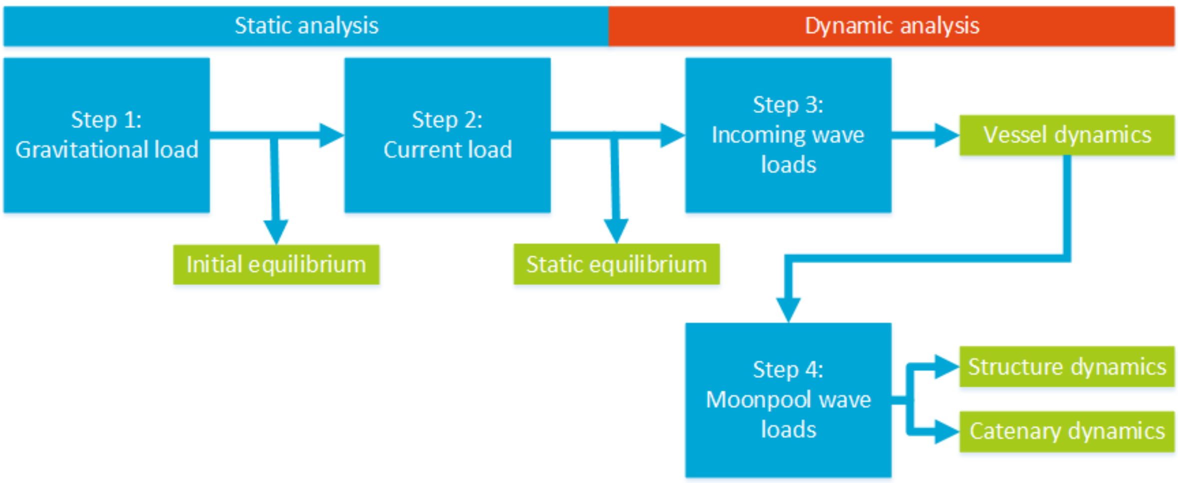

Figure 5.1: Enhanced analysis procedure model 1

5.1.2. MODEL 2: NON-EMPTY MOONPOOL CONDITIONS

In model 1, several assumptions are made with respect to the water motions in the moonpool. This leads to a reduction in accuracy of the model. If an increased accuracy is preferred, a more complete and extensive method should be used to calculate the dynamic behaviour of the system. From chapter 4 it is known that structures present in the moonpool do affect the water flow. To which extend a structure affects this behaviour depends on the type of structure. Due to a lack of measurements during structures in the moonpool, reliable RAO's could not be derived for non-empty moonpool conditions. Prior to the analysis, a CFD study should be done on how the moonpool behaves for a particular structure. This could be computationally extensive though.

A second assumption from model 1 that could be challenged is the way the moonpool wave is defined. Although the orbital behaviour is eliminated by setting the horizontal hydrodynamic properties to zero, the exponential decrease of the water particle motion over depth is not taken into account. This exponential decrease is valid for incoming waves, but the water in the moonpool can be considered as a moving solid mass of water. As a result, the water motions at the inlet of the moonpool are similar to the water motions at the surface. In model 1, this behaviour is not included, and the water motions at the bottom of the moonpool are therefore underpredicted. Consequently, the loads on the structure are underpredicted as well. The following procedure is proposed for a more accurate analysis:

1–2. Similar to model 1.

3. Determine the response of the moonpool for a particular structure by means of a CFD study. The timetrace of this response is used to calculate the hydrodynamic force on the buoy/other structures in the moonpool by using Morison's equation in a numerical calculation (i.e. Python or Matlab). The calculated force timetrace on the structure(s) is then given to Flexcom as point loads on these structure. The original wave spectrum can be used by Flexcom to calculate the vessel motions and the loads on structures that are not affected by the moonpool.

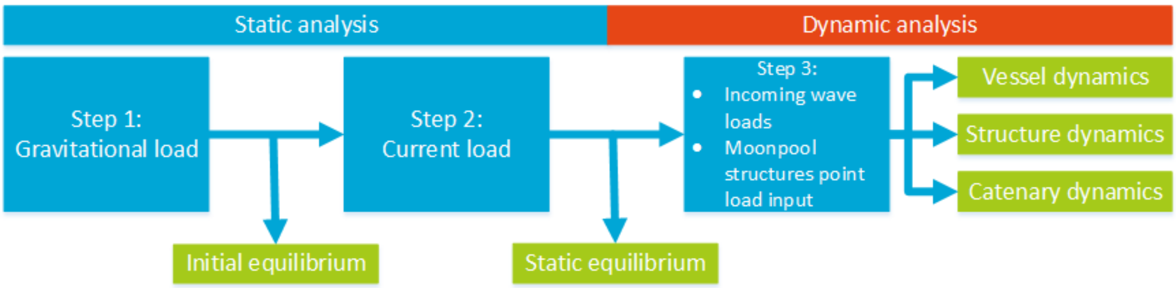

Figure 5.2: Enhanced analysis procedure model 2

Although the proposed procedure 2 should be more accurate, it does not necessarily mean model 1 gives bad results. Due to the exponential decrease of water motions over the depth of the moonpool, the wave kinematics at the bottom of the moonpool are underpredicted. However, this effect is to a certain extent compensated by the fact that empty moonpool conditions are considered. From figure 4.16 it is known that empty moonpool conditions are in fact an over-prediction of the real motions. Here the weight-compensation buoy blocks 16% of the moonpool inlet, but reduces the water motions significantly.

5.2. ADDITIONAL CHANGES

Implementing the moonpool into the Flexcom model mainly consists of separating the dynamics of the vessel from the dynamics of the structures. This represents reality to a certain extent, but in order to obtain even better results, some additional changes are applied to the model.

5.2.1. HORIZONTAL DAMPING

To eliminate the horizontal load component on structures in the moonpool, the hydrodynamic coefficients of the structure are set to zero. This reduces the excitation on the structure, but also reduces the damping of the structure motion. Although the structure is not excited by the water anymore, it is still connected to the vessel and can be excited in it's horizontal plane. As the structure is not damped in it's horizontal plane anymore, energy could build up and lead to resonance problems. In reality, the water in the moonpool would act as a damper and dissipate energy from the structure. To account for the damping of the structures, horizontal damper elements are added between the structure and a non-physical point somewhere far from the vessel. The damping force exerted by these elements are defined as

$$F_{damp} = -\left(C_0 + C_1 u + C_2 u^2\right) \tag{5.1}$$

where

C_0 :Constant damping coefficient $[-]$

C_1 :Linear damping coefficient $[-]$
C_2 :Quadratic damping coefficient $[-]$

These coefficients are based on the drag coefficients of the buoy. As the motions in the horizontal plane should be rather low, the use of the linear damping coefficient should suffice.

5.2.2. HYDRODYNAMIC COEFFICIENTS

As stated in section 3.4.2 the hydrodynamic properties of a structure change when the fluid flow around it is confined. As the moonpool of DCV Aegir is rather large compared to conventional structures, the blockage factor is low. In most of the cases the coefficients are not influenced to a large extent by the correction factor, but it should be applied for completeness.

5.3. VALIDATION

In order to validate the proposed models, the models are run using measured sea states of one of the 18" ILT installations. For all 18"-glsILT installations, measurements of the loads in the travelling block have been recorded. However, during only one of these installations the moonpool water motions have been measured while the weight compensation buoy was present. Unfortunately, no CFD data is available for either of the installations. Therefore, procedure 2 can only be validated by comparison with one installation. It is this installation that is used for the validation for both procedure 1 and procedure 2.

5.3.1. MODEL CONFIGURATION

The initial focus of this thesis was to investigate the particular load case where the buoy, ILT and catenary were connected to both the crane and the travelling block. In reality this load case is limited to a 1-minute time frame though. During the subsequent step, where the crane has been disconnected from the buoy, the excitation mechanism of the system is similar. The buoy is still in the same place, which means that the hydrodynamic loads on the buoy are still governed by the water motions in the moonpool. This configuration exists for at least half an hour, which provides a significant amount of load measurements. This gives a better opportunity to compare the measured travelling block loads with loads predicted by Flexcom. Therefore, for validation purposes, this configuration is chosen to be more suitable than the original load transfer configuration. As can be seen from figure 5.3, the crane wire is paid out such that the catenary load is taken by the travelling block and the ILT weight is taken by the buoy. On this configuration, model 1 and model 2 are applied respectively for a simulation time of 1300 seconds (100 seconds ramp-up time + 20 minutes).

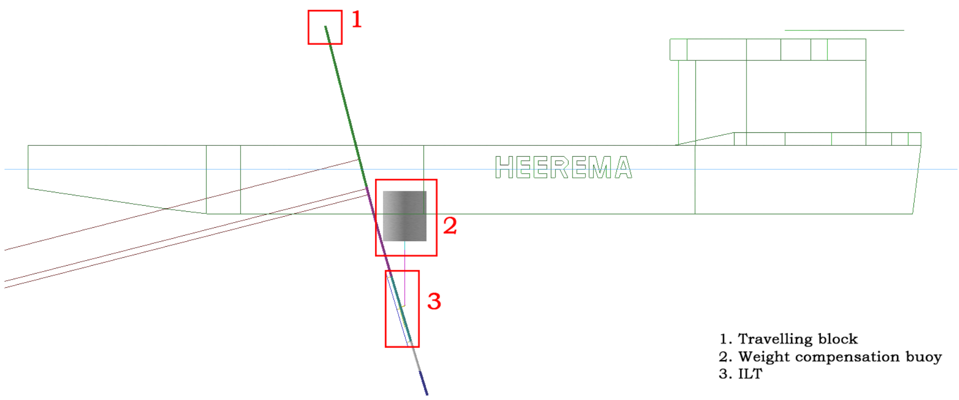

Figure 5.3: Flexcom model without crane and buoy in the moonpool

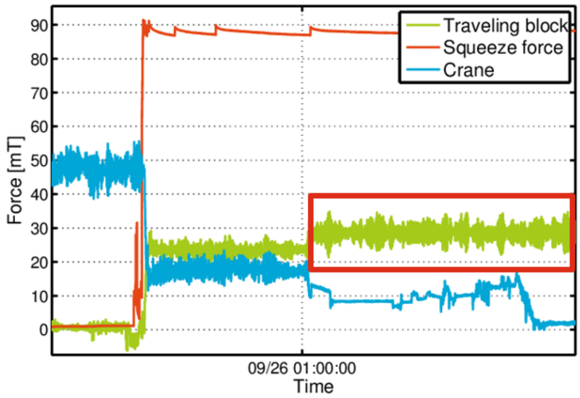

(a) Time-traces of offshore measurements

CONFIDENTIAL

(b) Spectral density of the measured force in the travelling block

Figure 5.4: Offshore load measurements of the travelling block

5.3.2. RESULTS

A summary of statistical values from both the offshore measurements and the two new procedures is given in table 5.1. As time traces are hard to compare qualitatively, the results are depicted in spectral density plots in figure 5.5. The spectral density plot and according time-trace are depicted in figure 5.4. For reference, the travelling block load time-traces generated by Flexcom can be found in appendix **??**. In order to compare the loads statistically, the mean and standard deviation are looked at first. However, as the purpose of these analyses is to determine whether certain limits are not exceeded, the P90 and P10 values are also calculated. These represent the upper 10% and lower 10% load limits.

	Measured	Procedure 1	Procedure 2
Static load component [mT]	28.5	28.4	28.4
σ of dynamic component [mT]	2.1	2.3	2.1
P90 max. exceedance load [mT]	32.8	32.3	32.5
P10 min. exceedance load [mT]	24.3	23.9	24.2

Table 5.1: Measured loads vs. calculated loads by procedure 1 and 2

Both procedure 1 and 2 do well resemble the measured loads in the travelling block. However, the spectral density plots in figure 5.5 show some differences. In procedure 1, next to the expected energy peak around the moonpool resonance frequency, shows energy at lower frequencies. These frequencies correspond to the vessel motions. The buoy loads using procedure 1 are calculated in Flexcom by the interaction between the imposed waves and the vertical hydrodynamic properties of the buoy. A part of the vessel motions is translated through these vertical hydrodynamic properties and observed in the measured loads. In procedure 2, all hydrodynamic properties are set to zero. Therefore, loads resulting from the vessel motions are not observed in procedure 2. Comparing the spectral density plots of procedure 1 and 2 to that of the actual force measurements show that energy from vessel motions is indeed not observed. The similarity between procedure 2 and the measured force spectrum proves that procedure 2 is indeed a more realistic approach. The use of procedure 2 does require specific knowledge about the real moonpool motions though.

(a) Model 1

(b) Model 2

Figure 5.5: Spectral density plots of the load in the travelling block in Flexcom for the validation configuration

5.3.3. ORIGINAL CONFIGURATION CHECK

Now that the proposed models are validated and proven to be able to predict loads accurately, the proposed procedures are applied on the original load transfer model. Although the 1-minute load-transfer operation is not a statistically relevant amount of time, the results of the analysis should be within the same range of the few load measurements that are available. The applied sea state is the one that was encountered during the GS1E ILT-installation. As the measured load in the travelling block cannot be compared by its standard deviation or P90 load exceedance values, the maximum and minimum load are used. These can be found in table 5.2.

	Proc. 1	Proc. 2
Static load component [mT]	0.68	0.63
σ of dynamic component [mT]	2.6	2.2
P90 max. exceedance load [mT]	6.3	4.6
P10 min. exceedance load [mT]	-4.6	-3.4

(a) Flexcom results

	Measured
Static load component [mT]	1.16
Maximum load [mT]	5.3
Minimum load [mT]	-2.6

(b) Measurement results

Table 5.2: Measured vs. simulated load for the load transfer configuration

Although the spectral peaks of the travelling block loads generated by Flexcom are comparable (figure 5.6, there is more energy in the spectrum of procedure 1. The peaks are wider and thus resulting in larger amplitudes. Accordingly, from table 5.2 can be seen that the P90 value of procedure 1 is 1.7 mT higher than the P90 value resulting from procedure 2. Comparing these values with the measured maximum during the load transfer, it can be concluded that procedure 1 in this case is slightly overestimating the dynamic loads on the travelling block. The results of procedure 2 however do compare really well when accounting for a static load shift of 0.53 mT.

5.4. CURRENT INFLUENCE

During all previously conducted analyses, the influence of current has been neglected as the dynamic behaviour of the system was of interest. However, from chapter 2 it is known that current influences the static load in the upper stem significantly. As the eventual analysis should include a current load, it is chosen to apply the most severe current case – the one coming from 180° direction –. In figure 5.7 the green line represents the static load in the upper stem when no current is applied. This is, as expected, a compressive load of 14 mT. The red line in the graph is the load calculated with the original model without the implementation of

CONFIDENTIAL

(a) Procedure 1

CONFIDENTIAL

(b) Procedure 2

Figure 5.6: Spectral density plots of the load in the travelling block during the load transfer in Flexcom

the moonpool. In the enhanced model, the current results in a static compression of 16.7 mT. The fact that the buoy is shielded by the moonpool results in a significant reduction in static load. In the original model the buoy encountered the full current flow, which leads to high loads.

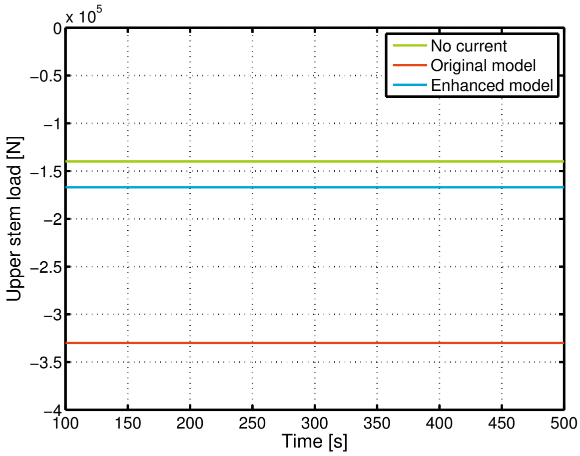

Figure 5.7: Current influence on the enhanced model

5.5. WORKABILITY

Concluding from the previous chapters, the loads in the travelling block are largely reduced by including the moonpool in the analysis procedure. This is partly due to the fact that the horizontal component of the orbital water motions does not excite the object in the moonpool anymore (piston mode). However, the major part of the reduction is due to the fact that the energy of the moonpool spectrum is in general less than the energy of the incoming wave spectrum. The amount of energy present in the moonpool spectrum is strongly dependent on the peak period of the moonpool RAO. In case the energy of the incoming wave spectrum lies outside of the resonance peak range of the RAO, the energy in the moonpool will be lower and thus workability is increased when comparing to the original model. There are cases though, where the peak period of the incoming wave spectrum is close to the resonance period of the moonpool. If so, the motion amplitude of the moonpool could be higher than the incoming wave height. This would induce higher loads on objects in the moonpool than one would expect from a simulation where the moonpool is not accounted for. In this case the original model would underestimate the loads. In order to avoid unexpected wait-on-weather, it should be investigated which regions of the world are sensitive for unfavourable moonpool resonance behaviour.

6

Conclusions and recommendations

6.1. Conclusion

In section 1.3 the objective for this thesis is formulated: Increase the understanding of mechanisms leading to compression in the upper and upper-counter stem during 18" ILT-installations and improve the model to increase workability. In this chapter, the conclusions with respect to this objective are drawn.

6.1.1. Moonpool

By systematically investigating the Flexcom model used for the installation of 18" ILT structures it became clear that the governing load leading to compression in the upper stem was the hydrodynamic loading of the buoy. As the buoy compensating the weight of the ILT-structure is hanging in the moonpool, the buoy was shielded from the outside wave field. However, this effect was not taken into account during the installation analysis. As the water in the moonpool is only excited by a small range of frequencies, generally the water motions in the moonpool are smaller than those of the outside wave field. This is confirmed by offshore measurements of the water motions in the moonpool. The following can be concluded with respect to the moonpool:

- In order to correctly calculate the hydrodynamic loads on structures in a moonpool, the moonpool water motions should be taken into account.
- Hydrodynamic loads on structures in a moonpool are inertia dominated and are well described by the inertia term of Morison's equation.
- Objects affect the motion behaviour of water in the moonpool. Viscous damping increases, leading to lower motion amplitudes. Additionally, the natural period of the moonpool tends to get longer.
- The water in the moonpool is excited by hull pressure fluctuations at the location of the moonpool. Only energy around the moonpool resonance period is let through.
- The higher the incoming wave, the lower is the relative response of the water motions in the moonpool due to an increase in viscous damping.
- The response of water motions in the moonpool are wave direction dependent. Head seas tend to excite the moonpool less than beam waves.
- Incoming waves with wave lengths which are a multiple of the length of the vessel lead to pressure interference patterns along the vessel. This influences the excitation of the moonpool, depending on its location.
- Diffraction software, such as WAMIT, is able to accurately predict the resonance period of the moonpool. However, due to the lack of viscous damping in these software packages, the response is overestimated.

6.1.2. MODEL ENHANCEMENT

In order to increase the accuracy of the structure installation analysis, the moonpool has been implemented in the original Flexcom model. Two enhancement procedures have been proposed. With respect to this implementation, the following conclusions can be drawn:

- The implementation of the moonpool results in loads which are in accordance with offshore load measurements in the travelling block.
- When hydrodynamic properties in the horizontal plane are set to zero, horizontal damping elements should be introduced in order to avoid resonance phenomena of the buoy.
- The current induced load on the buoy in the original model resulted in high static loads in the travelling block. Shielding of the moonpool reduces this effect.
- In order to obtain the best results, structure specific motion behaviour in the moonpool should be studied by means of CFD or experiments. However, applying empty moonpool conditions yields a considerably good approximation.

6.2. RECOMMENDATIONS

In this study the behaviour of water motions in the moonpool has been studied. By filtering and processing of measurements of these motions, RAO's for the relative wave height in the moonpool have been developed. These RAO's describe the relation between the incoming wave amplitude and the motion amplitude in the moonpool for empty moonpool conditions. Studies at Marintek show that objects in the moonpool do affect its behaviour and in the few cases that an object is present in the moonpool, measurements indeed show a reduction in water motion and a shift in the natural period. However, this effect is related to both the blockage factor of the moonpool and viscous effects related to the structure shape. Therefore, this is a structure specific phenomenon. The proposed model enhancements are based on the measurements of the buoy and are consequently less accurate for other structures. In order to get to a more solid and robust model, the following recommendations are suggested:

- Conduct structure specific CFD studies to gain insight in the real water motions in the moonpool during structure installation.
- As CFD calculations are computationally expensive, a more favourable method to calculate the response of the moonpool would be by means of diffraction software. However, viscous damping is not accounted for. This causes severe resonance overestimations of the water in the moonpool. Common practice is to reduce the response by using a so called damping lid. More knowledge about the viscous damping should be gained to model this lid however.
- Although the moonpool provides shielding for most of the sea-states, some sea-states with energy around the moonpool resonance period could lead to high amplitudes in the moonpool. This could badly affect the workability. Knowing upfront which regions are sensitive to such responses is preferable.
- In order to avoid resonance in the moonpool, several measures can be taken to shift the resonance period of the moonpool. The most effective way to do so is altering the draft of DCV Aegir. Decreasing the draft could however lead to stability issues during installation. The relation between stability and improved workability should be studied.

BIBLIOGRAPHY

[1] J. M. J. Journée and W. W. Massie, *OFFSHORE HYDROMECHANICS,* (2001).

[2] A. B. Aalbers, *The water motions in a moonpool,* Ocean Engineering (1984).

[3] Det Norske Veritas, *Recommended Practice DNV-RP-H103,* (2011).

[4] O. M. Faltinsen, *Sea Loads on Ships and Offshore Structures,* (1990).

[5] Molin, *On the piston and sloshing modes in moonpools,* J. Fluid Mech **430**, 27 (2001).

[6] V. Dilk, *Characterization of DCV Aegir Moonpool in Operational Condition,* (2014).

[7] L. Aspelund Subsea, N. Bjørnar Pettersen, J. Visscher MARINTEK Trondheim, and N. Tor-Bjørn Idsøe Naess Subsea, *HYDRODYNAMIC FORCES ACTING ON OBJECTS IN A MOONPOOL,* .

[8] J. R. Morison, *The forces exerted by surface waves on piles,* Petroleum Transactions, AIME **189**, 149 (1950).

[9] Det Norske Veritas, *DNV-RP-C205 ENVIRONMENTAL CONDITIONS AND ENVIRONMENTAL LOADS,* (2007).

[10] M. Stiassnie and G. Dagan, *Wave diffraction by detached breakwaters,* Waterways, harbors and coastal engineering division (1972).

[11] A. Sharma, *Integration of Different Wave Forcing Formulations with Nearshore Circulation Models*, Ph.D. thesis, Texas A&M University (2010).

[12] L. Aspelund, T.-B. Idsøe Naess, and S. Jan Visscher, *Experimental Study on the Hydrodynamic Forces acting on Objects in a Moonpool,* (2013).

A
RAO CALCULATIONS

A.1. INCOMING WAVE SPECTRUM

The offshore wave rider buoy generates a directional wave spectrum each hour. This spectrum first has to be transformed into a 2D wave spectrum. To do so, for every hour the spectral energy of each frequency component is added up by

$$E_f = \sum_{\theta=0}^{360} E_{f,\theta}$$

where

θ :Wave direction [°]
E_f :Spectral energy per frequency [$\frac{m^2}{Hz}$]

resulting in a 2D spectrum containing the energy for each frequency.

A.2. MOONPOOL WAVE SPECTRUM

The water motions in the moonpool are measured with a sampling rate of 0.1 seconds. As the measurement usually contains a reasonable amount of noise, a data filtering function has been written using Matlab. This function filters out abnormal peaks in the data signal. Using the clean timetrace of the water motions, the spectral density is generated. Subsequently this spectral density, together with the incoming wave spectrum is used to generate the relative motion RAO's of the moonpool. For those parts of the spectrum that contain energy, this calculation is valid. However, outside of the energy regions, the values tend to zero. This leads to RAO values that tend to infinity. Therefore it is chosen to use a cut-off frequency of 0.08 Hz. The filter function and processing function can be found below.

A.2.1. DATA FILTER

```
% load moonpooldata.mat

meansig = mean(data);
stdsig = std(data);

limmin = mean(data)-2*std(data);
limmax = mean(data)+2*std(data);

for i= 1:length(data)
    if data(1,i)>limmax | data(1,i)<limmin
        if i == 1
        data(1,i) = meansig;
        else
        data(1,i) = data(1,i-1);
        end
```

```
    end
end
```

A.2.2. RAO FUNCTION

```
clear all; close all; clc;

addpath('\\alecto\techylei\Dep\CC-General\CoP\20CP110\ ...
    Tools_storage\Under_development\matlab\spectral\FrequencyDomainTools');

MPpad = '\\ALECTO\techylei\Dep\PG-SIP\17 Thesis\Motion behavior assessment of an 18 ...
    inch ILT structure\9. Data\Enviview for MP\MP';
TRIAXYSpad = '\\ALECTO\techylei\Dep\PG-SIP\17 Thesis\Motion behavior assessment of an ...
    18 inch ILT structure\9. Data\Enviview for MP\TRIAXYS';

MPfolders = dir(MPpad);
MPfolders = char({MPfolders.name});
MPfolders = MPfolders(3:end,:);
TRIAXYSfolders = dir(TRIAXYSpad);
TRIAXYSfolders = char({TRIAXYSfolders.name});
TRIAXYSfolders = TRIAXYSfolders(3:end,:);

RAOspec = cell((360/15)+1,8);

for ifolder = 1:size(MPfolders(:,1))
    MPfiles = dir([MPpad,'\',MPfolders(ifolder,:),'\','*.mat']);
    MPfiles = {MPfiles.name}';
    TRIAXYSfiles = dir([TRIAXYSpad,'\',TRIAXYSfolders(ifolder,:),'\','*.mat']);
    TRIAXYSfiles = char({TRIAXYSfiles.name});
    TRIAXYSfiles = cellstr(TRIAXYSfiles);
    disp([num2str(ifolder),' of ',num2str(size(MPfolders(:,1)))])

    for ifiles = 1:size(MPfiles)
        load([MPpad,'\',MPfolders(ifolder,:),'\',char(MPfiles(ifiles,:))])
        load([TRIAXYSpad,'\',TRIAXYSfolders(ifolder,:),'\',char(TRIAXYSfiles(ifiles,:))])

        if round(length(dtaOctday)/(5*60*60))==24 && length(dtaTRIAXYS.maxdens) == 24
            for i = 1:24
                leftbound = (i-1)*18000+1;
                rightbound = i*18000;
                if i == 24
                    [MPspecfreq,MPspecdens] = ...
                        specdens((leftbound:length(dtaOctday))/5,dtaOctday(3 ...
                        ,leftbound:length(dtaOctday))/100,pi/100);
                    MPhead = mean(dtaOctday(2,leftbound:length(dtaOctday)));
                else
                    [MPspecfreq,MPspecdens] = ...
                        specdens((leftbound:rightbound)/5,dtaOctday(3 ...
                        ,leftbound:rightbound)/100,pi/100);
                    MPhead = mean(dtaOctday(2,leftbound:rightbound));
                end
                MPspecfreq = MPspecfreq/(2*pi);
                imaxfreq = find(MPspecfreq ≥ 0.3,1,'first');
                MPspecfreq = MPspecfreq(1:imaxfreq);
                MPspecdens = MPspecdens(1:imaxfreq);

                MPspecdens(1:17) = 0;

                m0 = trapz(MPspecfreq(18:61),dtaTRIAXYS.totaldens{i, 1}(18:61)');
                Hs = 4*sqrt(m0);

                TRIhead = dtaTRIAXYS.headmax{i, 1}(25);
                realhead = MPhead-TRIhead+180;
                if realhead<0
                    realhead = realhead+360;
                end
                if realhead>360
                    realhead = realhead-360;
```

```
                end
                realhead=15*round(realhead/15);

                dat = dtaTRIAXYS.dat{i,1};

                RAOsquare = MPspecdens ./dtaTRIAXYS.totaldens{i, 1}(1:61);
                RAO = sqrt(RAOsquare);

                [¬,imax] = max(RAO);
                if(max(RAO)≤4 && RAO(end)≤0.5 && imax ≥21)
                    integerindex = int8((realhead/15)+1);
                    RAOspec{integerindex,1}(size(RAOspec{integerindex,1},1)+1,:) = RAO;
                    RAOspec{integerindex,8}(size(RAOspec{integerindex,8},1)+1,:) = Hs;

                end
            end
        end
        %        pause
        %        close all
        %        figure
    end
end
```

B

FREE SURFACE AND HULL PRESSURES OF WAMIT BARGE

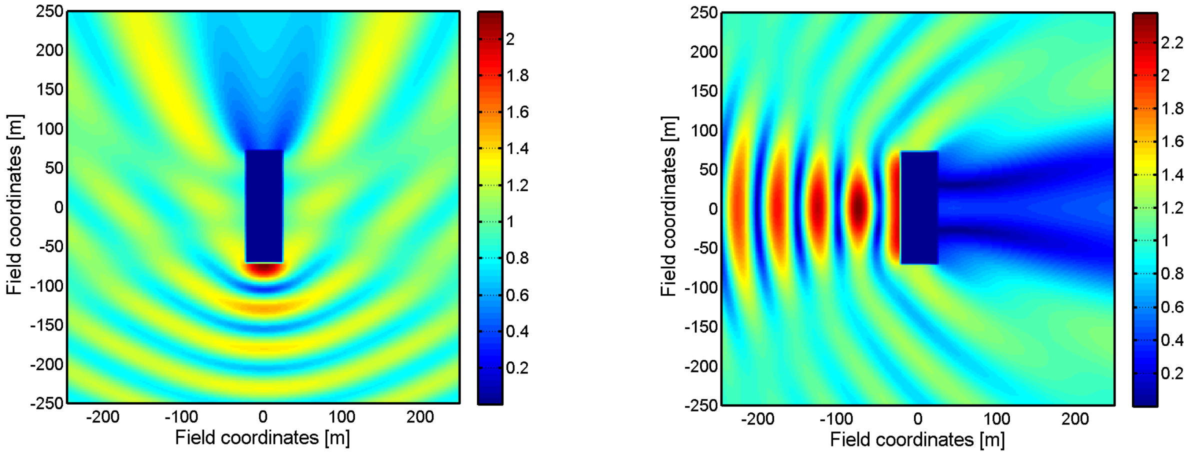

(a) Head waves

(b) Beam waves

Figure B.1: Surface elevation/pressure for a 144 m long barge

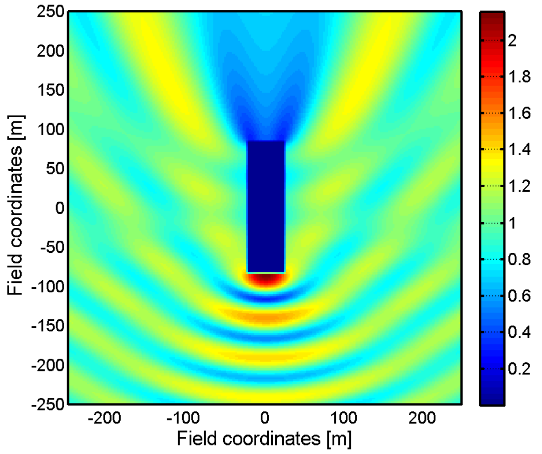

(a) Head waves

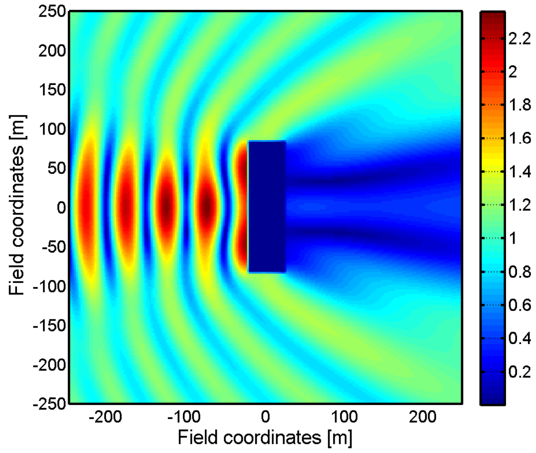

(b) Beam waves

Figure B.2: Surface elevation/pressure for a 168 m long barge

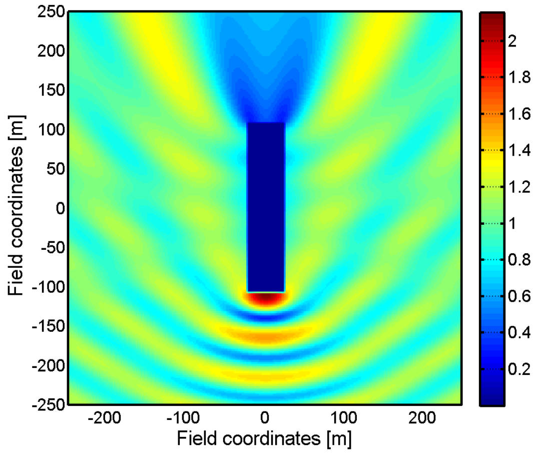

(a) Head waves

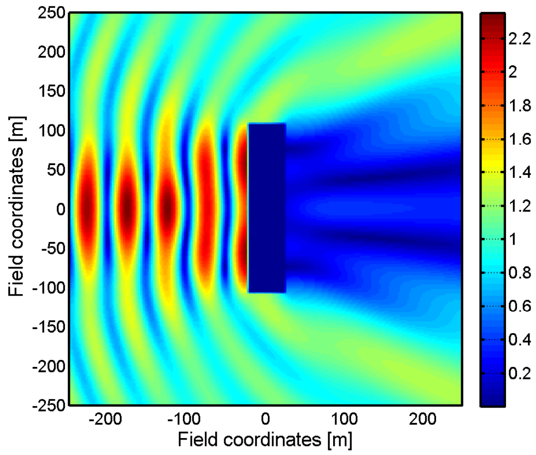

(b) Beam waves

Figure B.3: Surface elevation/pressure for a 216 m long barge

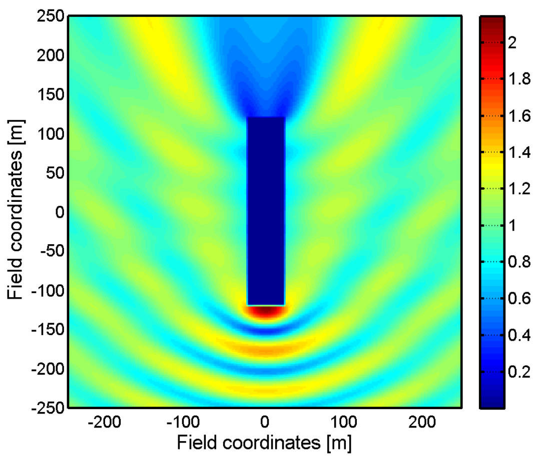

(a) Head waves

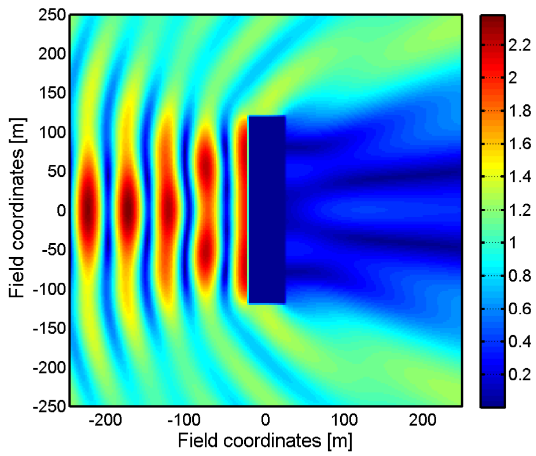

(b) Beam waves

Figure B.4: Surface elevation/pressure for a 240 m long barge

List of Figures

1 Current and wave directions w.r.t. DCV Aegir . . . xi
2 Flexcom axes . . . xi
3 Sign conventions w.r.t. loads . . . xii

1.1 Ichthys field . . . 1
1.2 ILT with buoyancy module . . . 2

2.1 Standard analysis procedure . . . 5
2.2 Flexcom model . . . 6
2.3 Offshore measurements . . . 6
2.4 Current influence for different directions . . . 7
2.5 Vessel motion influence on the load in the upper stem . . . 8
2.6 Spectral density plots of the upper stem load and the design wave spectrum . . . 9
2.7 Effect of the hydrodynamic loading of the submerged structures on the upper stem compression 10

3.1 Resonance modes of the moonpool . . . 11
3.2 Natural period of the moonpool of DCV Aegir . . . 14
3.3 Moonpool RAO's from model tests for specific wave directions . . . 15
3.4 A typical decay test . . . 16
3.5 2D plate definition . . . 17
3.6 Influence of objects in a moonpool on the moonpool RAO . . . 19

4.1 Incoming wave-spectrum . . . 21
4.2 Moonpool measurements . . . 22
4.3 Moonpool RAO . . . 23
4.4 Direction dependent moonpool RAO's . . . 23
4.5 Wave height dependency of the moonpool RAO . . . 24
4.6 Panel model of the DCV Aegir . . . 25
4.7 Moonpool response for every direction from WAMIT . . . 25
4.8 WAMIT barge models . . . 26
4.9 RAO's for WAMIT barge models . . . 27
4.10 Surface elevation for 96 m long barge . . . 28
4.11 Hull pressure distribution for 96 m long barge . . . 28
4.12 Hull pressure at moonpool location against barge length . . . 29
4.13 Surface elevation comparison between a 120 and 192 m barge ($T_p = 8s$) . . . 29
4.14 Surface elevation for the Aegir subject to beam waves ($T_p = s$) . . . 30
4.15 Hull pressure over the length of the ship with d the distance to the ship side . . . 30
4.16 Spectral density comparison between empty and non-empty moonpool conditions . . . 31

5.1 Enhanced analysis procedure model 1 . . . 34
5.2 Enhanced analysis procedure model 2 . . . 35
5.3 Flexcom model without crane and buoy in the moonpool . . . 36
5.4 Offshore load measurements of the travelling block . . . 37
5.5 Spectral density plots of the load in the travelling block in Flexcom for the validation configuration . . . 38
5.6 Spectral density plots of the load in the travelling block during the load transfer in Flexcom . . . 39
5.7 Current influence on the enhanced model . . . 39

B.1 Surface elevation/pressure for a 144 m long barge . . . 49
B.2 Surface elevation/pressure for a 168 m long barge . . . 50

B.3 Surface elevation/pressure for a 216 m long barge 50
B.4 Surface elevation/pressure for a 240 m long barge 50

List of Tables

2.1 Vessel motion comparison between Flexcom and offshore measurements 8

3.1 Moonpool specifications 14
3.2 Weight compensation buoy specifications 17
3.3 b/a ratio with corresponding C_a values 17
3.4 KC values with corresponding dominance 19

5.1 Measured loads vs. calculated loads by procedure 1 and 2 37
5.2 Measured vs. simulated load for the load transfer configuration 38